



Compound-specific carbon and hydrogen isotope analysis traces archaeal lipid signatures in cold seep marine systems

Katherine Keller^{a,*}, Sebastian Kopf^b, Jamie McFarlin^{b,c}, Ashley Maloney^b, Jeemin H. Rhim^d, Felix J. Elling^e, Kemi Ashing-Giwa^f, Isabel Baker^g, Amanda Calhoun^a, Ann Pearson^a

^a Department of Earth and Planetary Sciences, Harvard University, Cambridge, MA 02318, United States

^b Department of Geological Sciences, University of Colorado Boulder, Boulder, CO 80309, United States

^c Department of Geology and Geophysics, University of Wyoming, Laramie, WY 82071, United States

^d Department of Ecology, Evolution, and Marine Biology, University of California Santa Barbara, Santa Barbara, CA 93106, United States

^e Leibniz-Laboratory for Radiometric Dating and Isotope Research, Christian-Albrecht University of Kiel, 24118 Germany

^f Department of Geological Sciences, Stanford University, Stanford, CA 94305, United States

^g Department of Earth and Planetary Sciences, Johns Hopkins University, Baltimore, MD 21218, United States

ARTICLE INFO

Associate editor: Meixun Zhao

Keywords:

Isotopes

Hydrogen

Carbon

iGDGTs

Methane cycling

ABSTRACT

Compound-specific stable isotope analyses of archaeal lipid biomarkers can provide useful information on biogeochemical cycling in marine systems. While most work has focused on carbon isotopes, the analysis of hydrogen isotope ratios ($\delta^2\text{H}$) remains underexplored for its potential to characterize sources of lipids and metabolic diversity in marine sedimentary systems. This study examines the $\delta^2\text{H}$ values of archaeal biphytanes, derivatives of the parent isoprenoid glycerol dialkyl glycerol tetraether lipids (iGDGTs), as a tool to discriminate archaeal sources to sediments collected from Astoria Canyon, a cold-seep system along the Cascadia Margin. Using a mixing model applied to biphytane $\delta^2\text{H}$ values obtained from individual iGDGTs, we estimate the $\delta^2\text{H}$ signatures of the two primary endmember sources in this location: planktonic and benthic methane cycling communities. Additionally, we determine the structural biphytane combinations within each parent iGDGT. Our findings indicate that planktonic and benthic methane-cycling archaea both generate highly fractionated lipids, with modeled $\delta^2\text{H}$ signatures of -308 ‰ and -222 ‰ , respectively. When combined with reported compound-specific $\delta^{13}\text{C}$ values for the corresponding iGDGTs, the dual-isotope approach allows us to determine the mean $\delta^2\text{H}$ signatures of the two dominant archaeal communities, providing new endmember constraints for lipid source apportionment as well as the underlying biphytane structures comprising intact iGDGTs. These findings provide an interpretative framework for applying compound-specific stable isotopic approaches to disentangle sediment iGDGT sources and track methane cycling.

1. Introduction

The hydrogen isotopic composition ($\delta^2\text{H}$) of lipid biomarkers has emerged as an important analytical tool for studying past environments and ecosystems. Initial research on photoautotrophic organisms has established that lipid $\delta^2\text{H}$ signatures can be linked to their growth water, preserving a record of environmental water composition (Sachse et al., 2012). The relationships between metabolism, source water, and lipid $\delta^2\text{H}$ values provide unique potential for paleoenvironmental and ecological reconstructions. However, most of this research has

concentrated on eukaryotic and bacterial biomarkers, leaving a significant gap in the understanding and analysis of the $\delta^2\text{H}$ composition of archaeal lipids. Archaea play important roles in the marine biogeochemical cycles of carbon and nitrogen, and in oxygen-depleted sedimentary systems they play a critical role in methane cycling and the global methane budget (Knittel and Boetius, 2009). Due to analytical challenges, only a few studies have assessed the $\delta^2\text{H}$ composition of archaeal lipids. Most of this work has focused on cultured archaea (Kaneko et al., 2011; Wijker et al., 2019; Wu et al., 2020; Leavitt et al., 2023; Rhim et al., 2024), with limited analysis of archaeal lipids

* Corresponding author.

E-mail address: katherinekeller@g.harvard.edu (K. Keller).

<https://doi.org/10.1016/j.gca.2025.08.017>

Received 11 February 2025; Accepted 12 August 2025

Available online 15 August 2025

0016-7037/© 2025 Elsevier Ltd. All rights are reserved, including those for text and data mining, AI training, and similar technologies.

retrieved directly from environmental systems (Kaneko et al., 2011; Lengger et al., 2021).

The $\delta^2\text{H}$ signatures of bacterial lipid biomarkers are governed by metabolic processes and can be influenced by variations in metabolic rates and growth substrates (Dawson et al., 2015; Leavitt et al., 2023; Osburn et al., 2016; Zhang et al., 2009a). Modeling of lipid $\delta^2\text{H}$ patterns attribute the observed isotopic variability to kinetic isotope effects associated with specific pathways of hydrogen assimilation during biosynthesis, reflecting the selective incorporation of hydrogen from water into redox cofactors, such as NAD(P)H (Valentine et al., 2004; Zhang et al., 2009; Osburn et al., 2016; Wijker et al., 2019). It is generally believed that tradeoffs between biosynthetic demand and NADH and/or NADPH availability, associated with energy limitation, drive patterns of $\delta^2\text{H}$ fractionation in microbial lipids (Wijker et al., 2019). However, broad patterns of $\delta^2\text{H}$ fractionation observed in bacterial lipids distinguish autotrophic and heterotrophic organisms. Lipids from autotrophic organisms tend to be ^2H -poor, with $\delta^2\text{H}$ values ranging from -400 to -200 ‰ (Sessions et al., 2002; Valentine et al., 2004; Campbell et al., 2009; Zhang et al., 2009; Dawson et al., 2015; Osburn et al., 2016.). In contrast, the $\delta^2\text{H}$ values of lipids derived from heterotrophs tend to be richer in ^2H and exhibit a much larger range (-150 to $+300$ ‰) depending on growth substrate (Zhang et al., 2009; Wijker et al., 2019).

The $\delta^2\text{H}$ signatures and fractionation patterns of archaea are less understood compared to other organisms. Studies indicate that archaeal lipids are strongly ^2H -depleted (Kaneko et al., 2011; Dirghangi and Pagani, 2013; Lengger et al., 2014; Wu et al., 2020), resembling bacterial chemoautotrophs and eukaryotic photoautotrophs. Leavitt et al. (2023) observed a large, negative lipid-water fractionation (averaging -276 ‰) in the chemoautotrophic ammonia-oxidizer *Nitrosopumilus maritimus* and a distinct lipid-specific $\delta^2\text{H}$ pattern based on the number of internal cyclopentane rings, establishing a benchmark signature for planktonic, ammonia-oxidizing archaea. Similarly strong lipid-water fractionation has been reported in a few other chemoautotrophs, such as the methanogen *Methanosarcina barkerii* (-204 ‰ to -279 ‰ averaged across lipid types depending on methanogenesis substrate, Wu et al., 2020) and the metabolically flexible archaeon *Archaeoglobus fulgidus* (-249 to -228 ‰ for heterotrophy, -291 to -255 ‰ for autotrophy; Rhim et al., 2024). In contrast, heterotrophic archaea like *Haloarcula marismortui* and *Sulfolobus* spp. generally exhibit less fractionation (-103 to -228 ‰ and -213 to -161 ‰, respectively; Dirghangi and Pagani, 2013; Kaneko et al., 2011).

Estimates of lipid $\delta^2\text{H}$ from anaerobic methane-oxidizing archaea are limited to a few environmental studies and generally agree with the values above. Archaeal lipids from mediterranean cold-seep sediments exhibit $\delta^2\text{H}$ values between ca. -220 ‰ and -240 ‰ for iGDGTs -0 , -1 and -2 (Lengger et al., 2021); these values are ^2H -enriched compared to the planktonic archaeal representative *N. maritimus*, and more closely resemble laboratory methanogens and heterotrophs (Wu et al., 2020; Rhim et al., 2024). Based on these studies, the relatively distinct signatures of archaeal lipids suggest they could serve as indicators of metabolic pathways or in-situ biogeochemical processes. However, more studies are needed of both natural samples and model organisms to better understand the potential applications of archaeal lipid $\delta^2\text{H}$ analysis.

Here, we seek to fill in our understanding of archaeal lipid- H fractionation in a natural setting influenced by methane cycling by constraining the $\delta^2\text{H}$ signatures of archaeal lipids preserved in shallow marine sediments. We analyze $\delta^2\text{H}$ values of archaeal biphytanes (BPs) derived from purified parent iGDGTs collected from a cold-seep province in Astoria Canyon, Cascadia Margin. Recent research indicates the iGDGT assemblage from this site is dominantly a binary mixing system of planktonic and benthic methane-cycling archaea and establishes the $\delta^{13}\text{C}$ values of these two endmembers (Keller et al., 2025). We characterize the $\delta^2\text{H}$ signatures of these endmembers, presenting the first study measuring $\delta^2\text{H}$ values of BPs alongside $\delta^{13}\text{C}$ values of their

corresponding parent iGDGTs, isolated and purified through high-performance liquid chromatography (HPLC). Such dual-isotopic analysis of iGDGT $\delta^{13}\text{C}$ values paired with BP $\delta^2\text{H}$ values establishes an interpretive basis for fingerprinting multiple sources of iGDGTs in marine sediments and enables evaluation of the BP structures contributing to individual, intact iGDGTs, thereby linking molecular moieties with isotopic signatures.

2. Methods and materials

2.1. Sample information

Surface sediment samples were obtained from Cascadia Margin during cruise FK081824 (August-September 2018) using ROV SuBastian to collect 2 sediment cores with 7 depth intervals sampled per core. Shipboard multibeam technologies were used to locate sites with active bubbling; plumes of bubbles escaping the seafloor were visually confirmed remotely by the ROV camera feed. Samples were collected directly at the methane plume (samples S7, S9, S10, and S11) and approximately 20 m away (samples S1, S4, and S5) from the plume at Astoria Canyon ($-124^{\circ}39'$, $46^{\circ}13'$, 494 m water depth). Multiple cold-seep locations were sampled during the expedition (e.g., Keller et al., 2025), but this study focuses only on samples obtained from Astoria Canyon. The top 8 cm of the sediment was retrieved, and the core was partitioned in 1-cm or 2-cm depth intervals. Prior to isotopic analysis, samples were kept frozen at -20 °C, and approximately 10 % of the original material was archived. Depth intervals 1–2 cm and 6–8 cm were saved for future analysis. The remaining sediments (7 depth intervals per core) were used for lipid extraction.

2.2. Lipid extraction and biphytane collection

Samples were freeze-dried prior to lipid extraction (ca. 50 to 95 g of wet sediment). Total lipid extracts (TLEs) were obtained via microwave-assisted extraction using a CEM Mars™ system and separated by normal-phase high performance liquid chromatography (NP-HPLC; Fig. S1a,b) into individual iGDGTs as detailed in Keller et al. (2025). All iGDGT samples were assumed to have identical response factors in mass spectral quantification by atmospheric pressure chemical ionization mass spectrometry (Keller et al., 2025). Ether bonds of separated iGDGTs were cleaved in 57 % hydroiodic acid (HI) at 120 °C for 4 h. The resulting alkyl iodides were extracted with *n*-hexane and reduced to BPs using H_2 in the presence of a platinum (IV) oxide ($\text{Pt}(\text{IV})\text{O}_2$), following established methods (Kaneko et al., 2011). After filtering to remove the catalyst, BPs were purified over activated alumina (Al_2O_3). Biphytanes were identified using a quadrupole gas chromatography-mass spectrometer (GC-MS; Thermo ISQ LT with TRACE 1310) and quantified by GC-flame ionization detector (GC-FID; Thermo TRACE 1310) using the chromatographic program detailed below.

A portion of the original TLE was aliquoted for “bulk” $\delta^2\text{H}$ analysis. These samples underwent NP-HPLC cleanup to remove apolar and polar materials before ether cleavage and hydrogenation of the aggregate, bulk iGDGTs.

2.3. Hydrogen isotope analysis

Biphytane $^2\text{H}/^1\text{H}$ ratios were analyzed using an optimized methodology adapted from Leavitt et al. (2023). All measurements were made by gas chromatography pyrolysis isotope ratio mass spectrometry (GC-P-IRMS) on a GC IsoLink II IRMS System (Thermo Scientific), consisting of a Trace 1310 GC fitted with a programmable temperature vaporization (PTV) injector and a 30 m DB-5HT high temperature fused silica column (i.d. = 0.25 mm, 0.1 μm film thickness, max temperature 400 °C, Agilent Technologies), ConFlo IV interface, and 253 Plus mass spectrometer (Thermo Scientific). Samples were injected into a straight glass liner (2 mm I.D. \times 12 cm) with a quartz wool plug and after 1 min of rapid purge

flow of 40 mL/min He at 40 °C, analytes were transferred onto the GC column in splitless flow with 1.2 mL/min He using a fast ramp of the PTV from 40 °C to 450 °C in 6 min. After an initial hold at 40 °C for 1 min, the GC oven was ramped to 120 °C at 20 °C/min, followed by 15 °C/min to 345 °C and an isothermal hold at 345 °C for 5 min.

The $\delta^2\text{H}$ /H ratios are reported in delta notation ($\delta^2\text{H}$) in permil (‰) units relative to the international seawater standard on the VSMOW-SLAP (Vienna Standard Mean Ocean Water, Standard Light Antarctic Precipitation) scale. Peak areas (in volt seconds; Vs) refer to the time integrated and baseline subtracted peak amplitudes. Values of $\delta^2\text{H}$ were measured relative to the H_2 laboratory reference gas and then calibrated externally using a standard *n*-alkane mixture (A7, *n*C₁₆–*n*C₃₆; A. Schimmelmann, Indiana University; latest values from September 2024) plus C₃₆ *n*-alkane (*n*C₃₆, -259.2 ± 1.3 ‰ vs. VSMOW; A. Schimmelmann, Indiana University) which is more representative of biphytanes because it elutes between BP-0 and BP-1. The combined A7 and *n*C₃₆ standard was interspersed with the samples at regular intervals. The resulting hydrogen isotope calibration was performed in the R software package, based on 1788 compound-specific measurements of the combined A7 and *n*C₃₆ standard in 126 analyses with peak areas from 3.0 to 40.0 Vs using the following mass balance to correct for background, scale compression and peak-size effects:

$$\delta_x = \frac{A_{peak}}{A_{peak} - A_{bgd}} \cdot (\delta_{\text{H}_2} + \delta_{peak/\text{H}_2} + \delta_{\text{H}_2} \cdot \delta_{peak/\text{H}_2}) - \frac{A_{bgd}}{A_{peak} - A_{bgd}} \cdot \delta_{bgd}$$

The reference gas (δ_{H_2}) and background parameters (A_{bgd} and δ_{bgd}) were calculated from the standards. The δ_{H_2} value was estimated to be -309.9 ± 1.9 ‰ vs. VSMOW based on all standard compounds (Polissar and D'Andrea, 2014) and the calibration root mean squared error (RMSE) was 3.6 ‰. The uncertainty of the $\delta^2\text{H}$ measurements for individual biphytanes was determined based on the most conservative (i.e., largest) of the following: *i*) propagated error of the calibration (range: from 2.6 to 6.2 ‰); *ii*) bias-corrected pooled standard deviation of the samples (range: from 1.5 to 6.2 ‰); and *iii*) bias-corrected standard deviation of the *n*C₃₆ standard (4.2 ‰). Bias-corrections and standard deviation pooling were done as described in (Polissar and D'Andrea, 2014). The reported standard error of the mean (sem) for each compound/sample is based on the above-described most conservative standard deviations and the number of analytical replicates (s/\sqrt{n}).

The $\delta^2\text{H}$ values of the biphytanes were further corrected for H added during hydrogenation of alkyl iodides following methods and equations described in Leavitt et al. (2023) with an estimated isotopic composition of the added H of -676 ± 134 ‰ based on long-term internal measurements at CU Boulder (vs. -742 ± 177 ‰ previously estimated by Kaneko et al. 2011). The resulting hydrogenation correction shifted the $\delta^2\text{H}$ values of the biphytanes by +8.5 to +15.5 ‰ (depending on the number of rings) and increased analytical uncertainty by up to 2.1 ‰. The raw data and isotope calibration calculations are available in full on GitHub at github.com/KopfLab/2025_keller_et_al and make use of functionality provided by the *isoreader* (Kopf et al., 2021) and *iso-processor* R packages available at github.com/isoverse.

2.4. Biochemical stoichiometry of biphytanes

The optimal biochemical stoichiometry for the combinations of BPs per individual iGDGT was determined by a combinatorial optimization approach based on the observed relative abundance of biphytanes in NP-HPLC separated iGDGT samples. The BP stoichiometry has values of 0, 1, and 2, meaning any given BP may be present as a single moiety (1), two moieties (2), or absent (0) from any parent iGDGT (Fig. S2a,b).

While some iGDGTs have fixed stoichiometries – e.g., iGDGT-1 must contain one moiety of BP-0, one moiety of BP-1, and zero moieties of all other BPs – the higher-number iGDGTs allow for multiple combinations. For example, iGDGT-2 could contain BP-0 plus BP-2, or twice BP-1 (Fig. S2a,b). Thus, all possible configurations for each iGDGT were predefined in a stoichiometric matrix, and a model-generated Cartesian product for

the relative abundances of each BP was determined by normalizing the matrix rows to sum to 2, reflecting the stoichiometric contributions of two BPs per iGDGT. The relative abundances for each stoichiometric configuration were compared to the observed BP abundance distributions. Each combination was expressed as a fractional contribution (summing to 1), generating estimated distributions of biphytane combinations for each iGDGT parent. Equal proportions imply an equal possibility that each biphytane contributes to the iGDGT. For compounds that were not collected independently by NP-HPLC (e.g., iGDGT-4), the combinatorial approach could not be applied. In these cases, stoichiometric combinations were instead inferred from the isotopic model in combination with biphytane pairings per iGDGT (Fig. S2a,b). The co-elution of minor amounts of iGDGT-4 with crenarchaeol and iGDGT-3 enabled approximation of its BP stoichiometric combinations.

Combinatorial optimization was achieved by evaluating the root mean square error (RMSE) of each stoichiometric matrix against the observations, identifying the matrix with the lowest RMSE as the best fit. The resulting best-fit stoichiometric matrix (s) was subsequently used in the optimization of the $\delta^2\text{H}$ signature of each endmember (section 2.3).

2.5. Isotope mass balance model

We developed a forward optimization model to determine the consensus mean $\delta^2\text{H}$ signatures of the two previously established dominant archaeal endmembers (Keller et al., 2025): planktonic autotrophs and a broader group of benthic methanogenic and methanotrophic archaea. To model the $\delta^2\text{H}$ signatures and biphytane stoichiometry of the same endmembers, we combined newly measured $\delta^2\text{H}$ values and relative abundances of BPs (this study) with $\delta^{13}\text{C}$ measurements and endmember iGDGT distributions and $\delta^{13}\text{C}$ signatures from Keller et al. (2025). Methods for determining the $\delta^{13}\text{C}$ and relative distributions of intact iGDGTs are detailed in Keller et al. (2025).

Mean $\delta^2\text{H}$ values for planktonic and methane-cycling endmembers were determined by minimizing the RMSE between the observed and predicted $\delta^2\text{H}$ values across all samples using a linear isotope mixing equation:

$$\delta^2\text{H}_{k,j,predicted} = \frac{F_{p(i,j)} \delta^2\text{H}_{p,k} B_{p,k} + (1 - F_{p(i,j)}) \delta^2\text{H}_{m,k} B_{m,k}}{F_{p(i,j)} B_{p,k} + (1 - F_{p(i,j)}) B_{m,k}} \quad (1)$$

Eq. (1) calculates the $\delta^2\text{H}$ value for each biphytane (k) per iGDGT (j) in each sample (i). Here, m and p represent the benthic methane-cycling and planktonic endmembers, respectively.

The fractional contribution of planktonic archaea (F_p) for each sample was calculated using the endmember $\delta^{13}\text{C}$ signatures and $\delta^{13}\text{C}$ measurements of each sample (Keller et al., 2025):

$$F_{p(i,j)} = (\delta^{13}\text{C}_{i,j} - \delta^{13}\text{C}_m) / (\delta^{13}\text{C}_p - \delta^{13}\text{C}_m) \quad (2)$$

where $\delta^{13}\text{C}_m$ and $\delta^{13}\text{C}_p$ represent fixed $\delta^{13}\text{C}$ signatures of methane-cycling (−98 ‰) and planktonic (−19 ‰) endmembers, respectively, as determined by Keller et al. (2025).

The distribution of biphytanes (B) for each endmember (n) is derived using Eq. (3), which incorporates the iGDGT endmember distributions (X), i.e., the chromatographic profile associated with each endmember, from Keller et al. (2025) and the predefined, best-fit stoichiometric matrix (s):

$$B_{n,k} = \sum X_{n,j} \bullet s_{j,k} \quad (3)$$

Both the endmember distribution $X_{n,j}$, derived from Keller et al. (2025), and the stoichiometric matrix $s_{j,k}$, determined through a combinatorial fitting to observed BP abundances (see section 2.3), remained static throughout the optimization process. Consequently, the resulting matrix $B_{n,k}$ is fixed during the $\delta^2\text{H}$ optimization. Due to the presence of BP-4 in crenarchaeol and iGDGT-3 fractions, we assume a small methanotrophic iGDGT-4 endmember contribution (5 %) which

was not defined in Keller et al. (2025). Linear inverse mass-balance calculations were applied for adjacent iGDGTs (e.g., iGDGT-4 and crenarchaeol) to account for iGDGT co-elution in neighboring fractions (Supplemental Material S2a, Fig. S2a,b). To convert iGDGT distributions to BP distributions, B is multiplied by 0.5 to account for an individual BP compound, i.e., there are two BPs per iGDGT. A value of 0.5 represents an equal potential of that biphytane being one of the two components comprising an individual iGDGT.

The model optimizes for bulk BP endmember signatures (i.e., BP-0 through BP-4), effectively representing a mean signal, despite recent evidence demonstrating differences in $\delta^2\text{H}$ values for BPs with different numbers of internal cyclopentane rings (Leavitt et al., 2023). Model runs were initiated with $\delta^2\text{H}$ values randomly selected between -350 ‰ to -150 ‰, consistent with existing literature. We assessed the stability and variability of parameter estimates using bootstrapping (resampling with replacement; 5,000 iterations) and report the mean $\delta^2\text{H}$ values of each endmember that result in minimum RMSE, along with the confidence intervals (Fig. 4). The calculations and analyses were performed in Python and are available on Github at github.com/katherinekeller/astriacanyon-hydrogen-isotopes.

2.6. Assessing Agreement with Bulk Samples

We evaluated how well these optimized endmember $\delta^2\text{H}$ values explain the $\delta^2\text{H}$ values of total BP assemblages obtained from unseparated iGDGT fractions. Using pure endmember iGDGT profiles from Keller et al. (2025), we modeled hypothetical mixtures having planktonic endmember contributions ranging from 0 % to 100 % in 1 % increments. These mixtures were compared to the observed iGDGT distributions (chromatograms) from Keller et al. (2025) using the mean squared error (MSE) as a similarity metric. The mixture corresponding to the minimum MSE was identified as the best fit, and the resulting fractional contributions were used to predict the $\delta^2\text{H}$ values for the BPs obtained by ether cleavage of bulk samples by applying the inverted form of Eq. (1), utilizing the optimized $\delta^2\text{H}$ endmember values.

3. Results

3.1. $\delta^2\text{H}$ composition and relative abundances of biphytanes

The relative abundances of BPs are reported in Table 1 for individual iGDGTs and for bulk TLEs from which the iGDGTs were obtained. For the 7 sediment samples analyzed, 26 individual iGDGT fractions were separated and ether-cleaved, resulting in 55 $\delta^2\text{H}$ measurements of BPs from individual iGDGTs and 22 measurements of BPs from bulk sediment extracts (Table 3). Below, the data are reported according to the corresponding parent iGDGTs (Fig. 1).

3.1.1. iGDGT-0

All iGDGT-0 fractions exclusively contained BP-0 (Fig. 1). The $\delta^2\text{H}$ values of BP-0 associated with iGDGT-0 generally are the most ^2H -depleted among all BPs (Figs. 2, 3), with $\delta^2\text{H}$ values ranging from -327 to -278 ‰ (mean value of -308 ‰). Samples S1, S4, and S5 exhibit enriched ^2H -values (-302 ‰ to -278 ‰) compared to samples S7, S9, S10, and S11 (-327 ‰ to -315 ‰). In contrast, iGDGT-0 in samples S1, S4, and S5 is ^{13}C -depleted (ca. -60 ‰ to -40 ‰ for $\delta^{13}\text{C}$ of methane; (Pohlman et al., 2010; Joseph et al., 2013)) compared to samples S7, S9, S10, and S11 (ca. -35 ‰ to -25 ‰, Fig. 3). This pattern indicates that across all samples, archaeal compounds associated with benthic methane-cycling (e.g. iGDGT-1, -2), which are characterized by ^{13}C -depleted lipid signatures, consistently exhibit higher $\delta^2\text{H}$ values (Fig. 3).

3.1.2. iGDGT-1

Intact iGDGT-1 must be comprised of an equal ratio of BP-1 and BP-0 (Table 1), but here the collected iGDGT-1 fractions contained higher relative abundances of BP-0 compared to BP-1 (S5, S10, S11, Table 1).

Table 1

Relative abundances of individual BPs from individual iGDGTs and bulk samples. Samples with BPs which are missing or speculated to be associated with iGDGT-4 are indicated by *; a sample suspected of having partial TLE contamination is indicated by **.

Sample	iGDGT	BP-0	BP-1	BP-2	BP-3'	BP-4
S1	G0	1.00	—	—	—	—
	G2	0.28	0.50	0.22	—	—
	Cren*	0.02	—	0.51	0.47	—
S4	G0	1.00	—	—	—	—
	G2*	0.40	0.60	—	—	—
	Cren	—	—	0.51	0.49	—
	Bulk	0.55	0.16	0.17	0.12	—
S5	G0	1.00	—	—	—	—
	G1	0.65	0.35	—	—	—
	G2	0.33	0.47	0.20	—	—
	Cren	—	—	0.51	0.49	—
	Bulk	0.57	0.20	0.15	0.07	—
S7	G0	1.00	—	—	—	—
	G2	0.28	0.51	0.22	—	—
	Cren**	0.20	0.19	0.23	0.38	—
	Bulk	0.45	0.14	0.25	0.16	—
S9	G0	1.00	—	—	—	—
	G2	0.26	0.49	0.25	—	—
	G3*	0.09	0.36	0.48	—	0.06
	Cren*	—	—	0.53	0.45	0.01
	Bulk	0.41	0.22	0.26	0.10	0.01
S10	G0	1.00	—	—	—	—
	G1	0.61	0.39	—	—	—
	G2	0.26	0.49	0.25	—	—
	Cren	—	—	0.56	0.44	—
	Bulk	0.39	0.23	0.27	0.09	0.01
S11	G0	1.00	—	—	—	—
	G1	0.57	0.38	0.05	—	—
	G2	0.26	0.48	0.27	—	—
	G3*	0.06	0.35	0.52	—	0.08
	Cren	—	—	0.59	0.41	—
	Bulk	0.36	0.25	0.30	0.07	0.02

Specifically, the relative abundances of BP-0 and BP-1 are ca. 0.6 and 0.4, respectively, across all three sediment samples from which iGDGT-1 was collected. The $\delta^2\text{H}$ values for BP-0 are more negative than BP-1 (Fig. 2), with mean values of -255 ‰ and -228 ‰, respectively, yielding a mean difference of ca. 25 ‰ relative to BP-0, which is significantly larger than the expected 7 ‰ enrichment per ring that results from autotrophic biosynthesis (Leavitt et al., 2023). Here, both the stoichiometric and isotopic discrepancies reflect the mixing of end-member contributions caused by co-elution of iGDGT-0 within the iGDGT-1 fraction during NP-HPLC separation. The partial collection of iGDGT-0 leads to an overestimation of BP-0 abundances and affects the $\delta^2\text{H}$ values of BP-0 in proportion to the endmember representation in iGDGT-0 vs. iGDGT-1. We estimate by mass balance that approximately 30 % of the BP-0 signal in the iGDGT-1 fraction originates from iGDGT-0.

3.1.3. iGDGT-2

BP-0, BP-1, and BP-2 are detected in iGDGT-2, representing both structural BP combinations for this compound (Fig. S2a,b). The BPs have stoichiometrically proportional relative abundances that indicate minimal coelution with adjacent iGDGT structures. BP-0 and BP-2 have nearly equal relative abundances of approximately 0.25 each (with slight bias toward excess BP-0), representing one parent form of iGDGT-2 (Table 1). The relative abundance of BP-1 is roughly double, at

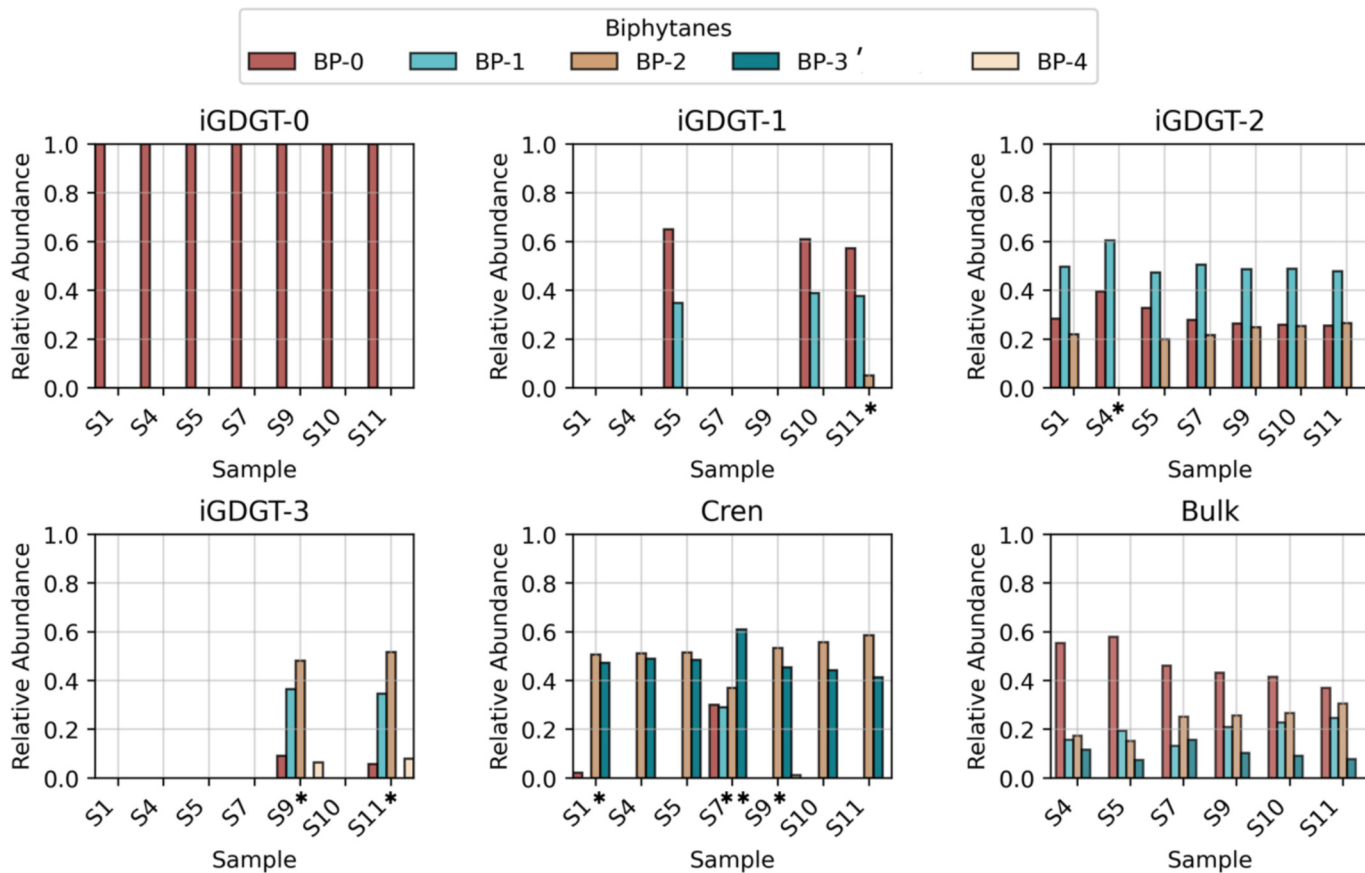


Fig. 1. The relative abundance of each BP within individual iGDGT fractions (as purified by NP-HPLC) and bulk extracts (last panel); x-axis labels denote samples. Variation between the two core locations (S1–5 and S7–11) reflect inter-core variability, and variation between samples collected away from the plume (S1–5) and at the plume (S7–11) reflect core depth variability. Due to sample loss, bulk sample S1 was excluded from relative abundance analysis. Asterisks denote samples which have missing or unexpected BPs (see Table 1); the double asterisk refers to a sample suspected of having partial TLE contamination. Partial co-elution of adjacent iGDGTs results in non-stoichiometric BP proportions in some samples, e.g., carryover of iGDGT-0 into the iGDGT-1 fraction yields excess BP-0 upon ether cleavage.

approximately 0.5 fractional abundance, representing the other parent form of iGDGT-2. Together, this implies that iGDGT-2 contains equal proportions of the structure containing two BP-1 sidechains and the structure containing a BP-0 sidechain alongside a BP-2 sidechain. By inference, therefore, the NP-HPLC chromatographic peaks iGDGT-2' and iGDGT-2, commonly observed as a leading minor peak followed by a trailing major peak, respectively (Becker et al., 2013), cannot be explained as differing in their underlying BP structure. Anomalous sample S4 contained only BP-0 and BP-1 in the iGDGT-2 fraction, presenting no feasible structural combination; this anomaly resulted from the presence of a co-eluting contaminant that prohibited peak integration at the retention time of BP-2.

The mean $\delta^2\text{H}$ values for BP-0, -1 and -2 are $-233\text{\textperthousand}$, $-221\text{\textperthousand}$, and $-218\text{\textperthousand}$, respectively (Fig. 2, Table 2). These $\delta^2\text{H}$ values follow the expected trend of more positive $\delta^2\text{H}$ values with additional internal cyclopentane rings and are within analytical error of the predicted 7 % biosynthetic enrichment per ring addition (Leavitt et al., 2023), suggesting that both source endmembers underlying iGDGT-2 conform to the biosynthetic pattern. Using a two-component mixing approximation (Eq. (2)), we estimate that the planktonic contributions to iGDGT-2 range from ca. 2 % to 20 % at Astoria Canyon, with the remainder attributed to the benthic-methane cycling archaea.

3.1.4. iGDGT-3

BP-0, -1, -2, and -4 were detected in the two obtained iGDGT-3 fractions (Table 1, Fig. 1). Notably, the all-cyclopentane form of BP-3 is below detection, suggesting it is an absent or trivial component of iGDGT-3. BP-1 and BP-2 are dominant, with mean fractional abundances

of ca. 0.35 and 0.50, respectively. We measure equal average abundances for BP-0 and BP-4 of 0.07, indicating partial collection of iGDGT-4 within the iGDGT-3 fraction. Alongside the observed excess of BP-2 relative to BP-1, stoichiometric mass balance indicates that approximately 25 % of the “iGDGT-3” fraction consists of co-collected iGDGT-4 and that this iGDGT-4 contains approximately equal parts of the structure containing two BP-2 chains and the structure containing one BP-0 and one BP-4 chain. The $\delta^2\text{H}$ values for BP-1 range from $-221\text{\textperthousand}$ to $-213\text{\textperthousand}$ and for BP-2 from $-219\text{\textperthousand}$ to $-217\text{\textperthousand}$, both with mean values of $-217\text{\textperthousand}$ (Figs. 1, 2). The average $\delta^2\text{H}$ difference between BP-1 and BP-2 is 3 %, smaller than the 7 % biosynthetic expectation. The differences between BP-1 and BP-2 likely are affected by variations in the underlying source endmember contributions to iGDGT-4 relative to iGDGT-3, which affects the $\delta^2\text{H}$ value measured for BP-2 (Table 2). Finally, the reported $\delta^2\text{H}$ values for BP-0 are $-273\text{\textperthousand}$ and $-288\text{\textperthousand}$, but these values likely contain analytical artifacts due to small peaks and low relative abundance (<0.10).

3.1.5. Crenarchaeol

In the crenarchaeol fractions, we detect BP-0, BP-2, BP-3' and BP-4 structures (Fig. 1, Table 1). Crenarchaeol is uniquely comprised of BP-2 and BP-3' chains, and the exclusive presence of BP-3' in these fractions indicates its diagnostic capability for crenarchaeol. We measure BP-2 in 6 % excess relative to BP-3', with mean percentage abundances of 53 % and 47 %, respectively. We detect BP-0 in sample S1 and BP-4 in sample S9, both in low abundances ($\leq 2\text{\%}$). The observed excess of BP-2 and presence of BP-0 and BP-4 indicates partial collection of iGDGT-4 in the crenarchaeol fractions. We estimate by stoichiometric mass balance

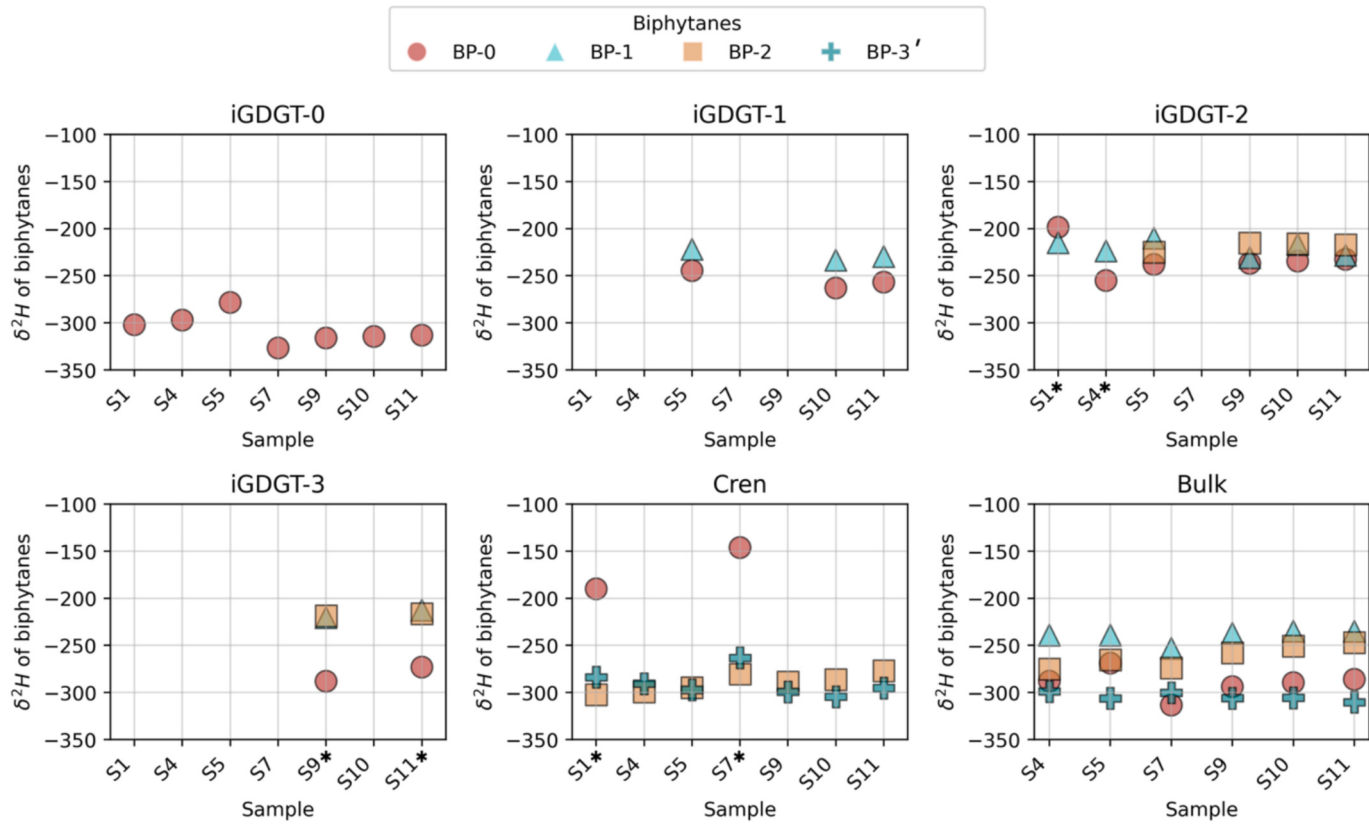


Fig. 2. The $\delta^2\text{H}$ values of each BP within individual iGDGT fractions (as purified by NP-HPLC) and bulk extracts (last panel); x-axis labels denote samples. Samples with missing or unexpected BPs are indicated by *. Variation between the two core locations (S1–5 and S7–11) reflect inter-core variability, and variation between samples collected away from the plume (S1–5) and at the plume (S7–11) reflect core depth variability. Due to sample loss, bulk sample S1 was excluded from $\delta^2\text{H}$ analysis.

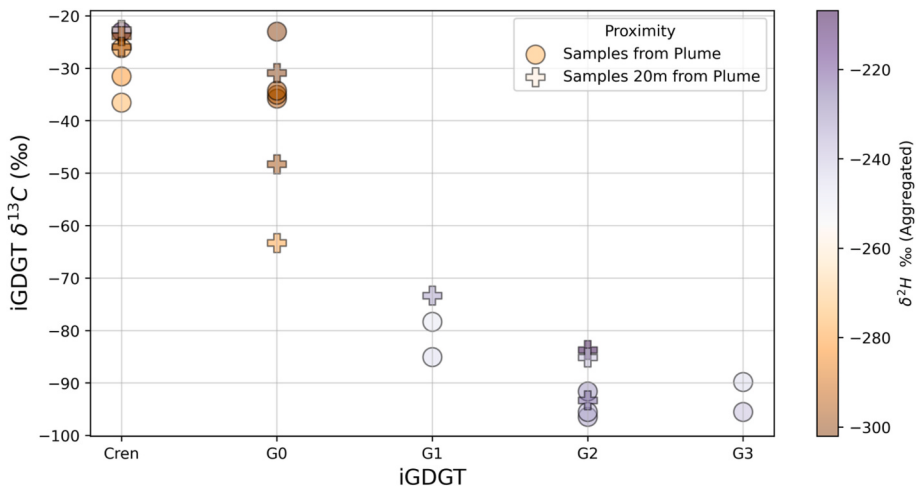


Fig. 3. Biphytane $\delta^2\text{H}$ values, grouped by $\delta^{13}\text{C}$ values of their corresponding intact iGDGTs (Keller et al., 2025). The colorbar represents the $\delta^2\text{H}$ values of the BPs, averaged across BPs for each iGDGT compound. The symbols indicate samples collected at different distances from the methane plume.

that iGDGT-4 represents approximately 10 % of the “crenarchaeol” fractions. These low fractional abundances prevent detailed analysis of BP structural combinations but are not inconsistent with the results obtained for the iGDGT-4 coeluting with iGDGT-3.

The $\delta^2\text{H}$ values for BP-2 is slightly more ^2H -enriched than BP-3, with mean values of -292 ‰ and -295 ‰ respectively (excluding outlier sample S7; Fig. 2). In individual samples, the mean difference between the two compounds is 13 ‰ . The data are inconsistent with the expected biosynthetic 7 ‰ enrichment expected for BP-3' due to its additional

internal ring, and these inconsistencies may again be due to iGDGT-4 contributions (reflecting the benthic methane endmember), which result in overabundant BP-2 and more positive BP-2 $\delta^2\text{H}$ values. Finally, sample S7 showed significant outlier results, with nearly equal and high abundances of BPs -0, -1, and -2, and anomalous isotopic results. This suggests contamination, perhaps by unseparated TLE, during sample processing and/or analysis; sample S7 was not included in subsequent endmember modeling.

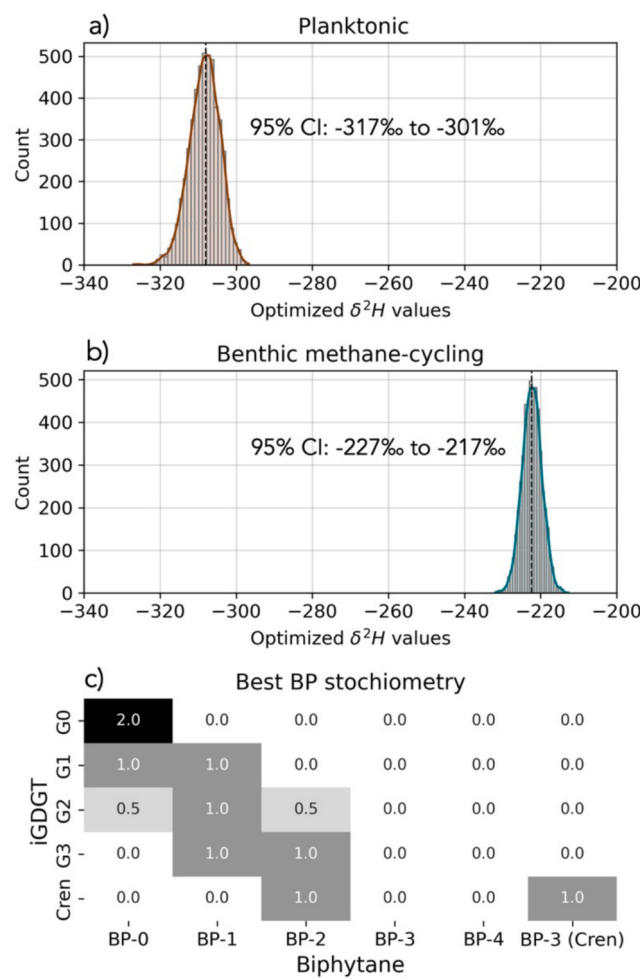


Fig. 4. Optimization results. A), B), Histograms of the $\delta^2\text{H}$ values for the planktonic and benthic methane-cycling endmembers, respectively, showing the distributions from bootstrapped sampling, with the black dashed lines representing the best fit $\delta^2\text{H}$ values. The model optimizes the $\delta^2\text{H}$ values for all BPs, providing an average representative value for each endmember. C) Heatmap showing best BP stoichiometries determined by combinatorial optimization. Each iGDGT contains 2 BPs, with iGDGTs 2 and 3 containing multiple possible combinations (Fig. S2a,b). The limited available data for BPs attributable to iGDGT-4 (see Table 1) are consistent with the stoichiometric combination: (0.5)BP-0: (1)BP-2: (0.5)BP-4, analogous to the pattern observed for iGDGT-2. BP-3' refers to the structure containing a cyclohexane ring (Schouten et al., 2002, 2013). All-cyclopentane BP-3 is below detection.

3.1.6. Biphytanes from bulk samples

The relative abundances and $\delta^2\text{H}$ values from unseparated sedimentary TLEs reflect a composite signal from the total iGDGT inventory. All samples exhibit similar patterns, with highest relative abundances measured for BP-0, with a mean value 0.45, followed by BP-1 and -2 measured in nearly equal proportion, of 0.20 and 0.24 respectively (Tables 1, 3). We measured the lowest fractional abundances of BP-3' (mean value of 0.17), consistent with low relative abundances of crenarchaeol (Keller et al., 2025) and detected BP-4 in very low relative abundance (<0.03) in samples S9, S10 and S11. Due to sample loss during the hydrogenation process, relative abundance and $\delta^2\text{H}$ measurements could not be conducted for sample S1.

The $\delta^2\text{H}$ values for BPs from bulk extracts are broadly consistent with the observed $\delta^2\text{H}$ values of BPs from the NP-HPLC separated iGDGT samples (Table 3). BP-1 and BP-2 have the most ${}^2\text{H}$ -enriched values, with mean values of -240 ‰ and -262 ‰ , respectively. The mean $\delta^2\text{H}$ value of BP-0 (-290 ‰) is more positive than BP-3'. Notably, we find that

Table 2

Mean $\delta^2\text{H}$ values of individual BPs from individual iGDGTs. Samples with BPs which are missing or speculated to be associated with iGDGT4 are indicated by *; a sample suspected of having partial TLE contamination is indicated by **. Relative abundances for the parent iGDGTs are reported from Keller et al. (2025).

Sample	iGDGT	iGDGT Relative Abundance	BP-0	BP-1	BP-2	BP-3'
S1	G0	0.39	-302 ± 5	—	—	—
	G2	0.16	-199 ± 6	-215 ± 6	—	—
	Cren*	0.31	-190 ± 5	—	-302 ± 5	-284 ± 5
S4	G0	0.48	-297 ± 4	—	—	—
	G2*	0.16	-255 ± 5	-224 ± 5	—	—
	Cren	0.22	—	—	-299 ± 6	-291 ± 6
S5	G0	0.44	-278 ± 4	—	—	—
	G1	0.16	-245 ± 5	-222 ± 5	—	—
	G2	0.23	-238 ± 5	-210 ± 4	-225 ± 5	—
S7	G0	0.42	-327 ± 4	—	—	—
	Cren**	0.29	-146 ± 6	-54 ± 6	-281 ± 6	-263 ± 6
	Cren	0.14	—	—	-295 ± 4	-297 ± 4
S9	G0	0.30	-316 ± 4	—	—	—
	G2	0.25	-237 ± 4	-231 ± 4	-215 ± 4	—
	G3*	0.12	-288 ± 5	-221 ± 4	-219 ± 4	—
S10	G0	0.27	-315 ± 4	—	—	—
	G1	0.11	-263 ± 4	-234 ± 4	—	—
	G2	0.27	-235 ± 4	-217 ± 4	-216 ± 4	—
S11	G0	0.25	-313 ± 4	—	—	—
	G1	0.12	-257 ± 5	-230 ± 4	—	—
	G2	0.28	-233 ± 4	-228 ± 4	-217 ± 4	—
S11	G3*	0.17	-273 ± 6	-213 ± 4	-216 ± 4	—
	Cren	0.15	—	—	-277 ± 5	-295 ± 5

the BP-3' is more ${}^2\text{H}$ -depleted in the bulk samples (mean value of -312 ‰) than in the NP-HPLC separated crenarchaeol samples (mean value of -305 ‰ , excluding sample S7). One possible explanation for this difference includes isotopic fractionation during separation of iGDGTs by NP-HPLC, resulting in more ${}^2\text{H}$ -depleted values in the case of incomplete collection of eluting peak tails (Smittenberg and Sachs, 2007).

Table 3

BP $\delta^2\text{H}$ values measured for bulk samples and predicted by the two endmember linear mixing model, compared to the mass-weighted net $\delta^2\text{H}$ values measured for these BPs in the individual iGDGTs.

Sample	Biphytane	Measured $\delta^2\text{H}$, Bulk TLE (‰)	Predicted $\delta^2\text{H}$, Bulk TLE (‰)	Mass-weighted $\delta^2\text{H}$, BPs from separated iGDGTs (‰)
S4	BP-0	-288 ± 6	-274	-294
	BP-1	-239 ± 6	-239	-224
	BP-2	-275 ± 6	-281	-299
	BP-3'	-299 ± 6	-307	-291
S5	BP-0	-269 ± 4	-257	-270
	BP-1	-239 ± 4	-230	-215
	BP-2	-265 ± 4	-264	-263
	BP-3'	-306 ± 5	-305	-297
S7	BP-0	-313 ± 6	-282	-327
	BP-1	-253 ± 6	-247	-
	BP-2	-274 ± 6	-292	-281
	BP-3'	-300 ± 6	-307	-263
S9	BP-0	-294 ± 4	-258	-301
	BP-1	-237 ± 4	-233	-229
	BP-2	-258 ± 4	-270	-254
	BP-3'	-308 ± 4	-305	-299
S10	BP-0	-290 ± 4	-254	-294
	BP-1	-235 ± 4	-231	-222
	BP-2	-251 ± 4	-264	-257
	BP-3'	-306 ± 4	-305	-305
S11	BP-0	-286 ± 4	-247	-288
	BP-1	-235 ± 4	-230	-226
	BP-2	-247 ± 4	-256	-241
	BP-3'	-310 ± 4	-303	-295

3.2. Modeling of $\delta^2\text{H}$ endmember values and distributions

Given the mixed endmember signals observed in the $\delta^2\text{H}$ data and prior $\delta^{13}\text{C}$ data (Keller et al., 2025), we developed a mixing model to quantify the isotopic signatures (Fig. 4a, b) and relative proportions of each endmember (Fig. 4c). The distribution and $\delta^{13}\text{C}$ values of iGDGTs in Astoria Canyon are attributed to two predominant archaeal sources: autotrophic planktonic communities and benthic methane-cycling communities, with negligible contribution from exogenous or in-situ heterotrophic archaea (Keller et al., 2025). For these two sources, we estimated the $\delta^2\text{H}$ signatures and BP stoichiometry per iGDGT using forward and combinatorial optimization models, respectively. Outliers (as identified in Table 2), including sample S7, were excluded from the model analyses to prevent bias in $\delta^2\text{H}$ endmember estimates.

The optimized $\delta^2\text{H}$ value for the planktonic endmember is ca. -308 ‰, while the benthic methane-cycling endmember shows an optimized $\delta^2\text{H}$ value of -222 ‰. Histograms representing 5000 bootstrapped iterations (Fig. 4a,b) exhibit gaussian-like structure for both endmembers indicating well-behaved parameter estimates and normally distributed uncertainty around the mean, with a relatively narrow 95 % confidence interval (CI) range for the methane-cycling endmember (-227 ‰ to -217 ‰) and the planktonic endmember (-317 ‰ to -301 ‰). The optimized model achieves a mean average error (MAE) of 11 %. Although the average analytical uncertainty for the BP $\delta^2\text{H}$ measurements is ± 5 ‰, the model does not account for biosynthetic ring effects of 7 ‰ per ring (observed in the model taxon *N. maritimus*; Leavitt et al., 2023). Consequently, the model MAE reflects both the analytical and the biosynthetic variability. Future research should aim to further investigate and include biosynthetic ring effects to improve $\delta^2\text{H}$ endmember signature estimates.

For iGDGTs with multiple potential BP combinations (e.g., iGDGT-

2), the model determines the combination that is most consistent with both the isotopic and relative abundance results (Fig. 4c, Fig. S2a,b). For iGDGT-2, the model indicates equal proportions of the structure containing BP-0 and BP-2 sidechains and the one containing two BP-1 sidechains. The absence of all-cyclopentane BP-3 indicates only one possible BP combination for iGDGT-3, consisting of a BP-1 and BP-2 sidechain. The structure of iGDGT-4 is not modeled, but BP abundance data for iGDGT-3 fractions (section 3.1.3) suggests it contains equal proportions of the combination of BP-0 with BP-4, and the combination with two BP-2 chains.

3.3. Bulk sample $\delta^2\text{H}$ predictions

To assess the validity of the optimized endmember $\delta^2\text{H}$ values, we compared the model-predicted $\delta^2\text{H}$ values of BPs with (i) the observed values from total BP assemblages obtained from unseparated (bulk) iGDGT fractions and (ii) the mass-weighted $\delta^2\text{H}$ values for BPs as measured from separated individual iGDGTs (Table 3). Our results demonstrate a generally good agreement across most BPs, with a mean average error (MAE) for all samples of 11 %. However, the linear model significantly overestimated the $\delta^2\text{H}$ values for BP-0 in samples where measurements were available (Table 3). The average MAE for BP-0 is 43 ‰, significantly larger than the MAE for BP-1 (6 ‰), BP-2 (6 ‰), and BP-3' (4 ‰).

These results indicate that the two-endmember system identified by Keller et al. (2025) effectively explains the distributions of BPs -1, -2 and -3' in Astoria Canyon sediments but does not sufficiently explain the sources of acyclic BP-0. The significant deviations for BP-0 suggest the presence of unaccounted-for sources of BP-0 that are not well represented by binary mixing of planktonic and benthic methane-cycling archaea. Future investigations should explore potential alternative sources or pathways contributing to BP-0 production and improve the model's representation of acyclic BPs.

4. Discussion

4.1. Endmember $\delta^2\text{H}$ estimates

A key objective of this work was to characterize both the absolute values and the variability in $\delta^2\text{H}$ signatures of archaeal lipids preserved in marine sediments. Determining the $\delta^2\text{H}$ endmember values allows for analysis of lipid-H fractionation in isoprenoid compounds, supporting their potential application in climate and paleoclimate proxies (Leavitt et al., 2023). The endmember values estimated for planktonic and benthic methane-cycling archaea in Cascadia Margin sediments are similar to or more ^2H -depleted than values reported for archaea in laboratory cultures. The nearly 100 ‰ difference in $\delta^2\text{H}$ signatures (-308 ‰ vs -222 ‰; Fig. 4) demonstrates the capability of $\delta^2\text{H}$ analyses to distinguish between these endmembers. Our results align with previous work establishing that archaeal lipids are characterized by systematically negative $\delta^2\text{H}$ values (Rhim et al., 2024). In bacteria, aerobic heterotrophs display a large range in H-isotope fractionation between lipid and water ($\epsilon_{\text{L/W}}$), spanning from -200 to +400 ‰ (Zhang et al., 2009; Wijker et al., 2019). Only a few chemoautotrophic organisms exhibit $\delta^2\text{H}$ values as negative as those observed in this study, in the case of fatty acids, highlighting the distinctiveness of such isotopic signals (Campbell et al., 2009; Zhang et al., 2009; Heinzelmann et al., 2015; Wu et al., 2020; Leavitt et al., 2023; Rhim et al., 2024). Strongly negatively $\delta^2\text{H}$ values of phytol in phytoplankton (<-350 ‰, Li et al., 2009; Rhim et al., 2024) suggest that such compounds represent better comparisons for isoprenoid lipids in future studies.

Fig. 5 illustrates the ability of dual isotope mixing to distinguish planktonic and benthic methane-cycling sources of archaeal lipids. Here, the $\delta^{13}\text{C}$ values represent values measured for iGDGTs (Keller et al., 2025), while the $\delta^2\text{H}$ values are for the BPs obtained from these iGDGTs. Most observations fall within the error envelope explained by linear, two

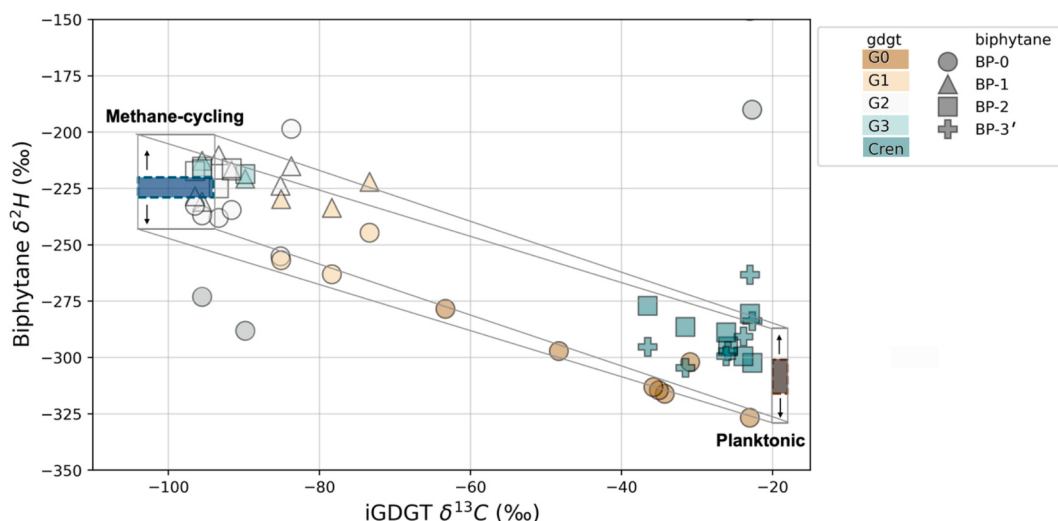


Fig. 5. Two-endmember linear mixing of BP and iGDGT isotope data ($\delta^2\text{H}$ vs. $\delta^{13}\text{C}$). The colored boxes represent the optimized endmember values, with the 95 % confidence intervals for the optimized $\delta^2\text{H}$ values. The box widths reflect the 94 % highest density intervals for the inferred $\delta^{13}\text{C}$ endmembers (Keller et al., 2025). The gray lines illustrate a hypothetical mixing space, extending vertically by $\pm 21 \text{ ‰}$ to account for potential biosynthetic ring effects (Leavitt et al., 2023). The gray-filled data points outside the mixing space represent analytical outlier measurements of small peaks of BP-0, likely associated with iGDGT-4, which are excluded from optimization calculations.

end-member mixing, with all values of BP-1 and some values of BP-0 and BP-2 (those associated with iGDGTs -1, -2 and -3) clustering near the benthic methane-cycling endmember. This suggests a shared origin, consistent with minimal planktonic contributions and estimates that 75 to 90 % of iGDGT-2 at this site originates from benthic methane cycling archaea (Table S1; Keller et al., 2025). In contrast, BP-3' and BP-2 derived from crenarchaeol cluster near the planktonic endmember, distinguished by ^2H -depleted and ^{13}C -enriched isotopic signals. While crenarchaeol is believed to be of exclusively planktonic origin, some samples plot in the range of ca. 80 % to 95 % planktonic (Table S1), reflecting co-elution of iGDGT-4 which affects the $\delta^{13}\text{C}$ value of the crenarchaeol iGDGT fraction. In addition, most BP-0 values associated with iGDGT-0 fall outside the proposed dual-isotopic mixing space.

There is skewness in the residuals (Figs. S1, Table S1), suggesting small but systematic biases in the model. The direction of this skew, however, indicates the $\delta^2\text{H}$ value of the planktonic endmember could be even more negative than the present result and thus the most highly fractionated archaeal signature observed to-date (Wu et al., 2020; Rhim et al., 2024). This is further supported by the bulk $\delta^2\text{H}$ values, where the model results (Table 3) do not sufficiently account for the measured $\delta^2\text{H}$ values of BP-0. This suggests the potential presence of an unaddressed third endmember primarily synthesizing acyclic iGDGTs and which was not detected in the $\delta^{13}\text{C}$ -based approach of Keller et al. (2025). Although our dataset is limited, the quality of the model fit (MAE) is similar to the analytical uncertainty of the $\delta^2\text{H}$ measurements, indicating that the results are robust despite these factors (Fig. S3). Future research should focus on increasing the number of $\delta^2\text{H}$ measurements to improve model fit and accuracy. Additionally, combining tandem $\delta^{13}\text{C}$ and $\delta^2\text{H}$ measurements could provide a more robust framework for identifying and resolving third endmembers that cannot be effectively distinguished using a single isotopic dimension. Finally, further investigation into the biosynthetic ring effects in different archaeal groups could enhance the model's accuracy and applicability. The current model is only designed to predict the average $\delta^2\text{H}$ signature across BPs, despite evidence showing that biosynthetic ring effects lead to more positive $\delta^2\text{H}$ values in compounds with internal cyclopentane rings (Leavitt et al., 2023).

4.2. Planktonic endmember $\varepsilon_{l/w}$ value

The model planktonic taxon, *N. maritimus* SCM1, yielded an average $\varepsilon_{l/w}$ value of $-266 \pm 9 \text{ ‰}$ for its average BPs (-276 ‰ for BP-0) across three growth rates in steady-state culture conditions (Leavitt et al., 2023). Assuming a $\delta^2\text{H}$ value near 0 ‰ for surface/subsurface seawater at Astoria Canyon, the $\varepsilon_{l/w}$ value modeled for the planktonic endmember in our study is nearly 50 % more ^2H -depleted. This might stem from inherent differences in physiology between the cultured *N. maritimus* and other pelagic ammonia-oxidizing archaea, or it may directly reflect differences in the geochemical conditions influencing growth. The magnitude of $\varepsilon_{l/w}$ in archaea can vary as a function of central metabolism and growth conditions. For example, Rhim et al. (2024) observed ca. 50 % variation in $\delta^2\text{H}$ values within *A. fulgidus* during experimental manipulations of carbon substrate and growth phase. While we assume the planktonic endmember to reflect obligate autotrophy, the marine community comprises multiple ecotypes, including Water Column A (WCA), Water Column B (WCB), and the coastal *Nitrosopumilus* clades, which preferentially inhabit different regions of the water column and exhibit distinct physiological and ecological characteristics (Santoro et al., 2019). Variations in marine habitats, time-varying methane fluxes at the bubble plume, and/or physiology could lead to differences in physicochemical factors that influence growth. The varying contributions from distinct ecotypes of planktonic archaea may collectively influence the $\delta^2\text{H}$ signal of sedimentary iGDGTs, reflecting the diversity of their ecological niches. Indeed, *N. maritimus* SCM1 differs from other coastal ammonia-oxidizing archaeal strains HCA1 and PS030 in its growth rate, optimal growth temperature, ammonia oxidation kinetics, and sensitivity to oxidative stress (Qin et al., 2014, 2015). Additionally, proteomic data for the pelagic, ammonia-oxidizing archaeon *Ca. Nitrosopelagicus brevis* (WCA) reveal distinct physiological and biochemical characteristics associated with this phylum (Santoro et al., 2015). Together, these examples highlight the biological diversity among pelagic ammonia-oxidizing archaea and indicate there may be further taxonomic variations in $\varepsilon_{l/w}$ values among the ammonia-oxidizing archaea. Finally, the temperature difference between the lab-grown *N. maritimus* (28°C) and the *in-situ* surface-temperature conditions in this region of the Northeast Pacific Ocean ($\leq 13^\circ\text{C}$; Boyer et al., 2018) may also play a role, as a normal kinetic isotope effect (KIE) is expected to cause increasingly ^2H -depleted signatures at lower

temperatures. However, the magnitude of the observed depletion is unlikely to be explained by temperature alone. More research is needed to explore $\delta^2\text{H}$ fractionation patterns among the diversity of planktonic ammonia oxidizing archaea, as well as the influence of temperature and other environmental factors.

4.3. Benthic methane-cycling endmember $\varepsilon_{\text{I/W}}$ value

The $\varepsilon_{\text{I/W}}$ value of the benthic methane cycling endmember may be nearly equivalent to the $\delta^2\text{H}$ value ($-222\text{\textperthousand}$), assuming a negligible isotopic difference between *in-situ* sediment porewaters and SMOW. Reports of interstitial porewaters at Cascadia Margin show a range in $\delta^2\text{H}$ values from $-10\text{\textperthousand}$ to $+20\text{\textperthousand}$ (Tomaru et al., 2006). These values would broaden the estimated $\varepsilon_{\text{I/W}}$ range to *ca.* -235 to $-205\text{\textperthousand}$.

While this endmember does not differentiate between organisms performing methanogenesis and methanotrophy, we speculate that the *ca.* $-222\text{\textperthousand}$ endmember $\delta^2\text{H}$ signature likely represents a primarily methanotrophic signal. Microbial methane oxidation occurs in the top few centimeters of Cascadia Margin sediments, similar to our sampling depth, as evidenced by steep sulfate-methane gradients and enriched $\delta^{13}\text{C}$ values of residual methane (Pohlman et al., 2010). Further, the high relative abundance of iGDGTs -1, -2 and -3 (Table 1, Keller et al., 2025), is consistent with production by certain groups of anaerobic methanotrophic (ANME) archaea (Zhang et al., 2011; Yoshinaga et al., 2015). Consortia of ANME communities (ANME -1, -2 and -3 clades) tend to dominate shallow cold water seep environments and have been shown to assimilate different forms of carbon, such as dissolved inorganic carbon and to a lesser extent methane (Blumenberg et al., 2005; Kellermann et al., 2012; Kurth et al., 2019). Methanogen lipid profiles typically are dominated by archaeol and acyclic iGDGTs (Koga and Nakano, 2008). Further, $\delta^2\text{H}$ values of archaeal lipids from a cultured methanogen range from -204 to $-279\text{\textperthousand}$, with more ${}^2\text{H}$ -depleted values associated with hydrogenotrophic methanogenesis (H_2/CO_2 reduction, Wu et al., 2020). Because methanogenesis in marine sediments is believed to dominantly occur via H_2/CO_2 reduction (Whiticar, 1999), this would represent a difference in $\varepsilon_{\text{I/W}}$ values of nearly $100\text{\textperthousand}$ between our methane-cycling endmember estimate and the signature of other methanogenic archaea, assuming that marine methanogenic archaea fractionate similarly to cultured methanogens (Wu et al., 2020). Thus, we propose that a methanogenic endmember may contribute to the production of an excess of ${}^2\text{H}$ -depleted BP-0 associated with iGDGT-0 in certain Astoria Canyon samples (e.g., S9–S11). In contrast, most BPs associated with iGDGT-1, -2, and -3 exhibit much more ${}^2\text{H}$ -enriched signatures and likely are associated with ANME-mediated methanotrophy (Fig. 5, Table 3).

Previous studies by Lenger et al. (2021) and Kaneko et al. (2011) provide the only reported $\delta^2\text{H}$ values of archaeal iGDGTs and archaeal BPs, respectively, that focus on methane-rich cold seep systems from natural environments. While both studies provide valuable insights, their limited $\delta^2\text{H}$ measurements (single measurements per compound) highlight the strength of our analysis, which benefits from a significantly larger sample size. Kaneko et al. (2011) report $\delta^2\text{H}$ measurements of BPs obtained from TLEs by ether cleavage, ranging from $-230\text{\textperthousand}$ to $-296\text{\textperthousand}$. Their $\delta^2\text{H}$ values for BP-1 and BP-2 of $-230\text{\textperthousand}$ and $-253\text{\textperthousand}$, respectively, resemble our bulk BP-1 and BP-2 mean $\delta^2\text{H}$ values of $-243\text{\textperthousand}$ and $-263\text{\textperthousand}$. The Lenger et al. (2021) study is more analogous to ours, measuring $\delta^2\text{H}$ values of intact, parent iGDGTs from Mediterranean methane seeps by high-temperature GC-IRMS approaches. They report ${}^2\text{H}$ -enriched values for iGDGT-1 and -2 (*ca.* $-220\text{\textperthousand}$), closely mirroring the $\delta^2\text{H}$ values of BPs associated with iGDGT-1 and -2 in Astoria Canyon. These similarities across studies suggest that the relatively ${}^2\text{H}$ -enriched signature for iGDGT-1 and -2 may be a robust indicator of benthic methanotrophic archaea, even across diverse marine environments.

One possible explanation for the significant differences in $\delta^2\text{H}$ values between ammonia-oxidizing (planktonic) and methanotrophic end-members could lie in the higher fluxes of reducing equivalents generated

during methane oxidation. These imbalances in reducing cofactors between anabolic and catabolic reactions are thought to drive the expression of a pronounced kinetic isotope effect, as observed in *N. maritimus* (Leavitt et al., 2023). Indeed, labeling experiments suggest that ANME have very low carbon utilization efficiencies, with 0.2–3 % of the carbon incorporated per reducing equivalent transferred to the syntrophic partner (Wegener et al., 2008, 2015, 2016), which could generate an imbalance of catabolic and anabolic fluxes. These experiments indicate that most of the biomass carbon in ANME archaea is derived from DIC via the Wood-Ljungdahl pathway instead of from methane (Kellermann et al., 2012; Wegener et al., 2016). Specifically, ANME archaea do not appear to use most of the $\text{CH}_3\text{-H}_4\text{MPT}$ derived from CH_4 oxidation for biomass generation (less than 3–15 % of CH_4 incorporated; Wegener et al., 2016). This suggests that ${}^2\text{H}$ fractionation in ANME organisms may be similar to that of other autotrophic, but non-methanotrophic, archaea that use the Wood-Ljungdahl pathway, such as *Archaeoglobus fulgidus* (Rhim et al., 2024). Differences in apparent fractionation between autotrophic vs. methanogenic archaea may result from the balance of catabolic and anabolic fluxes or from differential use of reducing cofactors, such as F_{420} during biosynthesis. Alternatively, isotopic exchange between methane and DIC during slow growth conditions may explain the similar isotopic signatures of methanotrophs and autotrophs. Further investigation of how physiological distinctions may account for the observed variability in $\delta^2\text{H}$ values across different archaeal groups is needed, especially for distinguishing between methanogenic, methanotrophic, and non-methane cycling Wood-Ljungdahl archaea.

Another source of relatively ${}^2\text{H}$ -enriched GDGTs are alkane-oxidizing archaea. C_2 to C_{5+} alkanes with enriched ${}^2\text{H}$ values (~-100 to $-120\text{\textperthousand}$) relative to methane ($\sim-140\text{\textperthousand}$) have been observed to comprise 15–32 % of the $\text{C}_1\text{-C}_{5+}$ alkanes at Cascadia Margin seeps (Pohlman et al., 2005). These alkanes may directly feed into biosynthesis pathways (Wegener et al., 2022), retaining some of the original H and thereby contributing to relatively ${}^2\text{H}$ -enriched GDGT $\delta^2\text{H}$ values.

4.4. Biosynthetic inferences and observations of biphytane stoichiometry

Zeng et al. (2019) demonstrated that cyclopentane rings of tetraethers are formed by the ring synthase proteins, GrsA and GrsB, each adding rings at distinct positions into the core iGDGT lipid. Their findings provide a powerful tool to predict sources of cyclized BPs within iGDGTs based on the presence of Grs homologs in the genome. Our observations and modeling results expand on these findings based on the observed stoichiometric combinations (Fig. 4c, Fig. S2a,b). We specifically identified two structural forms each for iGDGTs-2 and -4, with both forms occurring in nearly equal abundance within the parent iGDGTs. There is no apparent preference for the symmetric version of iGDGT-2 (two BP-1 moieties), with equal abundance observed for the version containing BP-0 alongside BP-2. While iGDGT-4 was not collected as a resolved fraction in NP-HPLC, minor quantities were recovered in the iGDGT-3 and crenarchaeol fractions. The presence of ether-cleaved products BP-4 and BP-0 in both fractions, coupled with the stoichiometric excess of BP-2 in those same fractions (Table 1), confirms that the two distinct structural forms again appear to be equally abundant: a symmetric form containing two BP-2 moieties and a highly asymmetric form containing BP-0 and BP-4 (Fig. S2a,b). The consistency of these stoichiometric patterns may imply a uniform archaeal source of iGDGT-2 and -4 compounds at this location. Importantly, synthesis of these BP structures requires different Grs proteins: GrsA is required for the synthesis of BP-1 and BP-2, while GrsB is required for the synthesis of BP-4 (Zeng et al., 2019). Given the stoichiometric uniformity among all samples analyzed here, it appears likely that the organism synthesizing iGDGTs-2 and -4 encodes and expresses both GrsA and GrsB. Culture experiments have demonstrated that individual organisms can express both proteins at varying levels, revealing differential transcriptional control of GrsA and GrsB (Zeng et al., 2019) and the requirement of GrsB

on prior expression of GrsA (Yang et al., 2023). The results here suggest that these differences are reflected specifically in the biosynthetic ratio of iGDGT-4/-2.

The absence of all-cyclopentane BP-3 in our samples suggests that this moiety is not a major biosynthetic product of tetraether-synthesizing marine archaea. Tentatively, this suggests that GrsB primarily acts in a dual or dimeric mechanism alongside GrsA, yielding two Δ^3 rings simultaneously rather than a single ring or sequential synthesis of two rings. In the Cascadia sediments, iGDGT-3 exclusively contains paired BP-1 and BP-2 sidechains, despite the theoretical possibility of the BP-0 plus BP-3 combination via GrsB expression (Fig. S2a,b). This finding aligns with other studies of marine samples that report only the cyclohexane-containing BP-3' (associated with crenarchaeol) in total BP assemblages (Hoefs et al., 1997; Wakeham et al., 2004). While our results cannot identify the taxonomic sources of cyclized iGDGTs, our analysis, combined with the approach by Zeng et al. (2019) and metagenomic analyses (e.g., Blum et al., 2023), may provide an effective method for understanding how BP combinations and the expression of Grs proteins relates to physiology, energetics and/or local ecology.

5. Potential applications

While the methane cycling endmember does not distinguish definitively between methanogenesis and methane consumption, we speculate that its $\delta^2\text{H}$ signature likely represents dominance of a methanotrophic community. Future analysis establishing the distinct $\delta^2\text{H}$ signatures of methanotrophic and methanogenic archaea, as well as further refinements on the variability of the iGDGT lipid profiles of these communities, could improve application of the dual-isotopic approach. Specifically, this framework may be used to track changes in the efficiency of the marine benthic methane filter, evaluating trends in archaeal benthic methane-cycling over geologic timescales (Sommer et al., 2006; Boetius and Wenzhöfer, 2013). The marine benthic methane filter, mediated by bacterial and archaeal methanotrophic communities, is estimated to consume over 90 % of subsurface methane fluxes before they reach the water column (Knittel and Boetius, 2009). These microbial communities play a crucial role in the marine methane budget, controlling atmospheric methane fluxes from marine systems (Reeburgh, 2007). While the marine methane budget is estimated to contribute 1 to 5 % of the global methane budget, the extent of these contributions could potentially be higher (Judd et al., 2002; Boetius and Wenzhöfer, 2013). Specifically, $\sim 10^7 \text{ Tg C}$ of methane may be stored in temperature-sensitive clathrate reservoirs, with the potential to be destabilized and released with rapid warming (Knittel and Boetius, 2009, references therein). As anthropogenic climate change is expected to increase global sea surface temperatures, the efficiency of the benthic methane filter and the extent to which methane will be consumed by microbial communities remains uncertain.

The dual-isotope approach used here also can serve as an additional metric to evaluate the reliability of GDGT-based sea surface temperature proxies, such as TEX_{86} , by providing a tool to help disentangle the heterogeneous inputs to marine sediments which can bias TEX_{86} -derived sea-surface temperature estimates (Keller et al., 2025). Current metrics to identify exogenous (methane and terrestrial-derived) iGDGT sources include the methane index (MI; Zhang et al., 2011) and branched vs. isoprenoid tetraether index (BIT; Hopmans et al., 2004), however the impacts of terrestrial and methanotrophic influences are highly variable, and universally applicable thresholds for each index are debatable (Zhang et al., 2011; Keller et al., 2025). $\delta^{13}\text{C}$ measurements of iGDGTs are useful to identify the presence of multiple sources to the sedimentary lipid pool, but quantitative estimates of source mixing can be difficult when, unlike in this work, $\delta^{13}\text{C}$ values of exogenous sources are similar to marine planktonic values (Pearson et al., 2016; Keller et al., 2025). Expanding the dual isotope approach to settings containing more than two endmembers will be a fruitful next step. For example, high-latitude terrigenous iGDGTs would be expected to be ^2H -depleted relative to

marine iGDGTs due to fractionation effects from evaporation and precipitation influencing terrestrial meteoric source waters (Sachse et al., 2012). Future analysis of high-latitude continental margin sediments could help to trace land-derived organic carbon delivery to marine systems.

Data availability

Raw data are available through GitHub at https://github.com/KopfLab/2025_keller_et_al.git. Model and Figures are also available through GitHub at <https://github.com/katherinekeller/astoriacanyon-hydrogen-isotopes.git>.

CRediT authorship contribution statement

Katherine Keller: Writing – review & editing, Writing – original draft, Visualization, Validation, Methodology, Investigation, Data curation, Conceptualization. **Sebastian Kopf:** Writing – review & editing, Methodology, Investigation, Formal analysis, Data curation. **Jamie McFarlin:** Writing – review & editing, Methodology, Investigation, Data curation. **Ashley Maloney:** Writing – review & editing, Methodology, Formal analysis, Data curation. **Jeemin H. Rhim:** Writing – review & editing, Writing – original draft, Investigation. **Felix J. Elling:** Writing – review & editing, Writing – original draft, Investigation. **Kemi Ashing-Giwa:** Writing – review & editing, Investigation, Data curation. **Isabel Baker:** Writing – review & editing, Data curation. **Amanda Calhoun:** Writing – review & editing, Formal analysis, Data curation. **Ann Pearson:** Writing – review & editing, Writing – original draft, Supervision, Investigation, Funding acquisition, Formal analysis, Conceptualization.

Declaration of competing interest

The authors declare that they have no known competing financial interests or personal relationships that could have appeared to influence the work reported in this paper.

Acknowledgements

We thank Peter Girguis for samples; Susan Carter for laboratory assistance; Mark Baum for helpful discussions on computational modeling; and Wil Leavitt for insightful feedback; and the GCA editorial staff, Alex Sessions, and two other anonymous reviewers for their instructive and helpful comments. Funding was provided by Harvard University, the US National Science Foundation (NSF) grant OCE-1843285 and the American Chemical Society Petroleum Research Fund (ACS-PRF) grant 66614-ND2 (AP); NSF grant EAR-1928303 (SHK); Deutsche Forschungsgemeinschaft grant 441217575 (FJE); and JHR was supported by GBMF9730 (to A. Santoro). We acknowledge the analytical contributions of the CU Boulder Earth Systems Stable Isotope Lab (CUBES-SIL) Core Facility (RRID:SCR_019300).

Appendix A. Supplementary material

The Supplementary Material includes Supplementary Texts S1–S2, Supplementary Table S1, Supplementary Figures S1–S3, and associated references. Text S1, links to data and code availability; Text S2a, chromatographic separation and collection of iGDGTs; Text S2b, iGDGT structures and theoretical combinations of biphytane moieties; Table S1, model input and output summary; Fig. S1, example chromatograms of Astoria Canyon samples using NP-HPLC; Fig. S2, structures of iGDGTs and biphytane components; Fig. S3, model diagnostics and evaluation. Supplementary material to this article can be found online at <https://doi.org/10.1016/j.gca.2025.08.017>.

References

- Becker, K.W., Lipp, J.S., Zhu, C., Liu, X.L., Hinrichs, K.U., 2013. An improved method for the analysis of archaeal and bacterial ether core lipids. *Org Geochem.* 61, 34–44.
- Blum, L.N., Colman, D.R., Eloe-Fadrosh, E.A., Kellom, M., Boyd, E.S., Zhaxybayeva, O., Leavitt, W.D., 2023. Distribution and abundance of tetraether lipid cyclization genes in terrestrial hot springs reflect pH. *Environ. Microbiol.* 25, 1644–1658.
- Blumenberg, M., Seifert, R., Nauhaus, K., Pape, T., Michaelis, W., 2005. In vitro study of lipid biosynthesis in an anaerobically methane-oxidizing microbial mat. *Appl. Environ. Microbiol.* 71, 4345–4351.
- Boetius, A., Wenzhöfer, F., 2013. Seafloor oxygen consumption fuelled by methane from cold seeps. *Nat. Geosci.* 6, 725–734.
- Boyer, Tim P., García, Hernán E., Locarnini, Ricardo A., Zweng, Melissa M., Mishonov, Alexey V., Reagan, James R., Weathers, Katharine A., Baranova, Olga K., Paver, Christopher R., Seidov, Dan, Smolyar, Igor V., 2018. World Ocean Atlas 2018.
- Campbell, B.J., Li, C., Sessions, A.L., Valentine, D.L., 2009. Hydrogen isotopic fractionation in lipid biosynthesis by H₂-consuming Desulfobacterium autotrophicum. *Geochim. Cosmochim. Acta* 73, 2744–2757.
- Dawson, K.S., Osburn, M.R., Sessions, A.L., Orphan, V.J., 2015. Metabolic associations with archaea drive shifts in hydrogen isotope fractionation in sulfate-reducing bacterial lipids in cocultures and methane seeps. *Geobiology* 13, 462–477.
- Dirghangi, S.S., Pagani, M., 2013. Hydrogen isotope fractionation during lipid biosynthesis by Haloarcula marismortui. *Geochim. Cosmochim. Acta* 119, 381–390.
- Heinzemann, S.M., Villanueva, L., Sinke-Schoen, D., Sinninghe Damsté, J.S., Schouten, S., van der Meer, M.T.J., 2015. Impact of metabolism and growth phase on the hydrogen isotopic composition of microbial fatty acids. *Front. Microbiol.* 6.
- Hoefs, M.J.L., Schouten, S., De Leeuw, J.W., King, L.L., Wakeham, S.G., Sinninghe Damsté, J.S., 1997. Ether lipids of planktonic archaea in the marine water column? *Appl. Environ. Microbiol.* 63, 3090–3095.
- Hopmans, E.C., Weijers, J.W., Schefuß, E., Herfort, L., Damsté, J.S.S., Schouten, S., 2004. A novel proxy for terrestrial organic matter in sediments based on branched and isoprenoid tetraether lipids. *Earth Planet. Sci. Lett.* 224 (1–2), 107–116.
- Joseph, C., Campbell, K.A., Torres, M.E., Martin, R.A., Pohlman, J.W., Riedel, M., Rose, K., 2013. Methane-derived authigenic carbonates from modern and paleoseeps on the Cascadia margin: mechanisms of formation and diagenetic signals. *Palaeogeogr. Palaeoclimatol. Palaeoecol.* 390, 52–67.
- Judd, A.G., Hovland, M., Dimitrov, L.I., García Gil, S., Jukes, V., 2002. The geological methane budget at continental margins and its influence on climate change. *Geofluids* 2, 109–126.
- Kaneko, M., Kitajima, F., Naraoka, H., 2011. Stable hydrogen isotope measurement of archaeal ether-bound hydrocarbons. *Org. Geochem.* 42, 166–172.
- Keller, K.J., Baum, M.M., Liu, X.L., Ashing-Giwa, K., Baker, I.R., Blewett, J., Pearson, A., 2025. Constraining the sources of archaeal tetraether lipids in multiple cold seep provinces of the Cascadia Margin. *Org. Geochem.* 200.
- Kellermann, M.Y., Wegener, G., Elvert, M., Yoshinaga, M.Y., Lin, Y.S., Holler, T., Mollar, X.P., Knittel, K., Hinrichs, K.U., 2012. Autotrophy as a predominant mode of carbon fixation in anaerobic methane-oxidizing microbial communities. *Proc. Natl. Acad. Sci.* 109, 19321–19326.
- Knittel, K., Boetius, A., 2009. Anaerobic oxidation of methane: progress with an unknown process. *Annu. Rev. Microbiol.* 63, 331–334.
- Koga, Y., Nakano, M., 2008. A dendrogram of archaea based on lipid component parts composition and its relationship to rRNA phylogeny. *Syst. Appl. Microbiol.* 31 (3), 169–182.
- Kopf, S., Davidheiser-Kroll, B., Kocken, I., 2021. Isoreader: an R package to read stable isotope data files for reproducible research. *J. Open Source Softw.* 6 (61), 2878.
- Kurth, J.M., Smit, N.T., Berger, S., Schouten, S., Jetten, M.S.M., Welte, C.U., 2019. Anaerobic methanotrophic archaea of the ANME-2d clade feature lipid composition that differs from other ANME archaea. *FEMS Microbiol. Ecol.* 95.
- Leavitt, W.D., Kopf, S.H., Weber, Y., Chiu, B., McFarlin, J.M., Elling, F.J., Hoeft-McCann, S., Pearson, A., 2023. Controls on the hydrogen isotope composition of tetraether lipids in an autotrophic ammonia-oxidizing marine archaeon. *Geochim. Cosmochim. Acta* 352, 194–210.
- Lenger, S.K., Lipsewers, Y.A., De Haas, H., Sinninghe Damsté, J.S., Schouten, S., 2014. Lack of 13C-label incorporation suggests low turnover rates of thaumarchaeal intact polar tetraether lipids in sediments from the Iceland shelf. *Biogeosciences* 11, 201–216.
- Lenger, S.K., Weber, Y., Taylor, K.W.R., Kopf, S.H., Berstan, R., Bull, I.D., Mayser, J.P., Leavitt, W.D., Blewett, J., Pearson, A., Pancost, R.D., 2021. Determination of the δ²H values of high molecular weight lipids by high-temperature gas chromatography coupled to isotope ratio mass spectrometry. *Rapid Commun. Mass Spectrom.* 35.
- Li, C., Sessions, A.L., Kinnaman, F.S., Valentine, D.L., 2009. Hydrogen-isotopic variability in lipids from Santa Barbara Basin sediments. *Geochim. Cosmochim. Acta* 73 (16), 4803–4823.
- Osburn, M.R., Dawson, K.S., Fogel, M.L., Sessions, A.L., 2016. Fractionation of hydrogen isotopes by sulfate- and nitrate-reducing bacteria. *Front. Microbiol.* 7, 1–16.
- Pearson, A., Hurley, S.J., Walter, S.R.S., Kusch, S., Lichtin, S., Zhang, Y.G., 2016. Stable carbon isotope ratios of intact GDGTs indicate heterogeneous sources to marine sediments. *Geochim. Cosmochim. Acta* 181, 18–35.
- Pohlman, J.W., Bauer, J.E., Waite, W.F., Osburn, C.L., Chapman, N.R., 2010. Methane hydrate-bearing seeps as a source of aged dissolved organic carbon to the oceans. *Nat. Geosci.* 4, 37–41.
- Pohlman, J.W., Canuel, E.A., Chapman, N.R., Spence, G.D., Whiticar, M.J., Coffin, R.B., 2005. The origin of thermogenic gas hydrates on the northern Cascadia Margin as inferred from isotopic (13C/12C and D/H) and molecular composition of hydrate and vent gas. *Org. Geochem.* 703–716.
- Polissar, P.J., D'Andrea, W.J., 2014. Uncertainty in paleohydrologic reconstructions from molecular δD values. *Geochim. Cosmochim. Acta* 129, 146–156.
- Qin, W., Amin, S.A., Martens-Habbena, W., Walker, C.B., Urakawa, H., Devol, A.H., Ingalls, A.E., Moffett, J.W., Armbrust, E.V., Stahl, D.A., 2014. Marine ammonia-oxidizing archaea isolates display obligate mixotrophy and wide ecotypic variation. *Proc. Natl. Acad. Sci.* 111, 12504–12509.
- Qin, W., Carlson, L.T., Armbrust, E.V., Devol, A.H., Moffett, J.W., Stahl, D.A., Ingalls, A.E., 2015. Confounding effects of oxygen and temperature on the TEX86 signature of marine Thaumarchaeota. *Proc. Natl. Acad. Sci.* 112, 10979–10984.
- Reeburgh, W.S., 2007. Oceanic methane biogeochemistry. *Chem. Rev.* 107, 486–513.
- Rhim, J.H., Kopf, S., McFarlin, J., Maloney, A.E., Battner, H., Harris, C.M., Zhou, A., Feng, X., Weber, Y., Hoeft-McCann, S., Pearson, A., Leavitt, W.D., 2024. Metabolic imprints in the hydrogen isotopes of Archaeoglobus fulgidus tetraether lipids. *Geochim. Cosmochim. Acta* 386, 196–212.
- Sachse, D., Billault, I., Bowen, G.J., Chikaraishi, Y., Dawson, T.E., Feakins, S.J., Freeman, K.H., Magill, C.R., McInerney, F.A., Van Der Meer, M.T.J., Polissar, P., Robins, R.J., Sachs, J.P., Schmidt, H.L., Sessions, A.L., White, J.W.C., West, J.B., Kahmen, A., 2012. Molecular paleohydrology: interpreting the hydrogen-isotopic composition of lipid biomarkers from photosynthesizing organisms. *Annu. Rev. Earth Planet. Sci.* 40, 221–249.
- Santoro, A.E., Dupont, C.L., Richter, R.A., Craig, M.T., Carini, P., McIlvin, M.R., Yang, Y., Orsi, W.D., Moran, D.M., Saito, M.A., 2015. Genomic and proteomic characterization of "Candidatus Nitrosopelagicus brevis": an ammonia-oxidizing archaeon from the open ocean. *Proc. Natl. Acad. Sci.* 112, 1173–1178.
- Santoro, A.E., Richter, R.A., Dupont, C.L., 2019. Planktonic marine archaea. *Ann. Rev. Mar. Sci.* 13, 19.
- Schouten, S., Hopmans, E.C., Schefuß, E., Sinninghe Damsté, J.S., 2002. Distributional variations in marine crenarchaeotal membrane lipids: a new tool for reconstructing ancient sea water temperatures? *Earth Planet. Sci. Lett.* 204, 265–274.
- Schouten, S., Hopmans, E.C., Sinninghe Damsté, J.S., 2013. The organic geochemistry of glycerol dialkyl glycerol tetraether lipids: a review. *Org. Geochem.* 54, 19–61.
- Sessions, A.L., Jahnke, L.L., Schimmelman, A., Hayes, J.M., 2002. Hydrogen isotope fractionation in lipids of the methane-oxidizing bacterium *Methyloccoccus capsulatus*. *Geochim. Cosmochim. Acta* 66 (22), 3955–3969.
- Smittenberg, R.H., Sachs, J.P., 2007. Purification of dinosterol for hydrogen isotopic analysis using high-performance liquid chromatography-mass spectrometry. *J. Chromatogr. A* 1169, 70–76.
- Sommer, S., Pfannkuche, O., Linke, P., Luff, R., Greinert, J., Drews, M., Gubsch, S., Pieper, M., Poser, M., Viergutz, T., 2006. Efficiency of the benthic filter: Biological control of the emission of dissolved methane from sediments containing shallow gas hydrates at Hydrate Ridge. *Global Biogeochem. Cycles* 20.
- Tomaru, H., Matsumoto, R., Torres, M., Borowski, W., 2006. Geological and geochemical constraints on the isotopic composition of interstitial waters from the Hydrate Ridge region, Cascadia Continental Margin. *Proceedings of the Ocean Drilling Program, Scientific Results*, 204, 1–20.
- Valentine, D.L., Sessions, A.L., Tyler, S.C., Chidthaisong, A., 2004. Hydrogen isotope fractionation during H₂/CO₂ acetogenesis: hydrogen utilization efficiency and the origin of lipid-bound hydrogen. *Geobiology* 2 (3), 179–188.
- Wakeham, S.G., Hopmans, E.C., Schouten, S., Sinninghe Damsté, J.S., 2004. Archaeal lipids and anaerobic oxidation of methane in euxinic water columns: a comparative study of the Black Sea and Cariaco Basin. *Chem. Geol.* 205, 427–442.
- Wegener, G., Krukenberg, V., Riedel, D., Tegetmeyer, H.E., Boetius, A., 2015. Intercellular wiring enables electron transfer between methanotrophic archaea and bacteria. *Nature* 526, 587–590.
- Wegener, G., Krukenberg, V., Ruff, S.E., Kellermann, M.Y., Knittel, K., 2016. Metabolic capabilities of microorganisms involved in and associated with the anaerobic oxidation of methane. *Front. Microbiol.* 7.
- Wegener, G., et al., 2022. Anaerobic degradation of alkanes by marine archaea. *Ann. Rev. Microbiol.* 73, 553–577.
- Wegener, G., Niemann, H., Elvert, M., Hinrichs, K.U., Boetius, A., 2008. Assimilation of methane and inorganic carbon by microbial communities mediating the anaerobic oxidation of methane. *Environ. Microbiol.* 10, 2287–2298.
- Whiticar, M.J., 1999. Carbon and hydrogen isotope systematics of bacterial formation and oxidation of methane. *Chem. Geol.*
- Wijker, R.S., Sessions, A.L., Fuhrer, T., Phan, M., 2019. 2H/1H variation in microbial lipids is controlled by NADPH metabolism. *Proc. Natl. Acad. Sci.* 116, 12173–12182.

- Wu, W., Meador, T.B., Könneke, M., Elvert, M., Wegener, G., Hinrichs, K.U., 2020. Substrate-dependent incorporation of carbon and hydrogen for lipid biosynthesis by *Methanoscarcina barkeri*. *Environ. Microbiol. Rep.* 12, 555–567.
- Yang, W., Chen, H., Chen, Y., Chen, A., Feng, X., Zhao, B., Zheng, F., Fang, H., Zhang, C., Zeng, Z., 2023. Thermophilic archaeon orchestrates temporal expression of GDGT ring synthases in response to temperature and acidity stress. *Environ. Microbiol.* 25, 575–587.
- Yoshinaga, M.Y., Lazar, C.S., Elvert, M., Lin, Y.S., Zhu, C., Heuer, V.B., Hinrichs, K.U., 2015. Possible roles of uncultured archaea in carbon cycling in methane-seep sediments. *Geochim. Cosmochim. Acta* 164, 35–52.
- Zeng, Z., Liu, X.L., Farley, K.R., Wei, J.H., Metcalf, W.W., Summons, R.E., Welander, P.V., 2019. GDGT cyclization proteins identify the dominant archaeal sources of tetraether lipids in the ocean. *Proc. Natl. Acad. Sci.* 116, 22505–22511.
- Zhang, Y.G., Zhang, C.L., Liu, X.L., Li, L., Hinrichs, K.U., Noakes, J.E., 2011. Methane Index: a tetraether archaeal lipid biomarker indicator for detecting the instability of marine gas hydrates. *Earth Planet. Sci. Lett.* 307, 525–534.
- Zhang, X., Gillespie, A.L., Sessions, A.L., 2009a. Large D/H variations in bacterial lipids reflect central metabolic pathways. *Proc. Natl. Acad. Sci.* 106 (31), 12580–12586.
- Zhang, Z., Sachs, J.P., Marchetti, A., 2009b. Hydrogen isotope fractionation in freshwater and marine algae: II. Temperature and nitrogen limited growth rate effects. *Org. Geochem.* 40, 428–439.

1 Appendix A. Supplemental Material.
2 Compound-specific carbon and hydrogen isotope analysis traces archaeal lipid signatures in cold
3 seep marine systems

5 Authors: Katherine Keller¹, Sebastian Kopf², Jamie McFarlin^{2,3}, Ashley Maloney², Jeemin H. Rhim⁴, Felix
6 J. Elling⁵, Kemi Ashing-Giwa⁶, Isabel Baker⁷, Amanda Calhoun¹, Ann Pearson¹

8 Affiliations: Department of Earth and Planetary Sciences, Harvard University, Cambridge, MA 02318¹,
9 Department of Geological Sciences, University of Colorado Boulder, Boulder, CO 80309², Department of
10 Geology and Geophysics, University of Wyoming, Laramie, WY 82071³, Department of Ecology,
11 Evolution, and Marine Biology, University of California Santa Barbara, Santa Barbara, California, 93106⁴,
12 Leibniz-Laboratory for Radiometric Dating and Isotope Research, Christian-Albrecht University of Kiel,
13 24118 Germany⁵, Department of Geological Sciences, Stanford University, Stanford, CA 94305⁶,
14 Department of Earth and Planetary Sciences, Johns Hopkins University, Baltimore, MD, 21218⁷

16 1. Data Availability.

17 Raw data: github.com/KopfLab/2025_keller_et_al

18 Model/Figures: github.com/katherinekeller/astoriacanyon-hydrogen-isotopes

20 2. iGDGT and biphytane background.

21 2a. iGDGT collection and composition. The iGDGT compounds analyzed in this study were first
22 isolated via NP-HPLC and further purified using RP-HPLC, following protocols established by Pearson et
23 al. (2016). These steps separate individual iGDGT compounds—e.g., iGDGT-1 from iGDGT-2—and
24 remove non-target organic compounds. Figure S1a demonstrates an example chromatogram of a NP-HPLC
25 separation. Separated iGDGTs are collected based on retention times of compound *m/z* ratios from
26 environmental standards. Standards are run at the beginning and end of every analysis to determine
27 compound elution timing and assess instrument drift and/or variability.

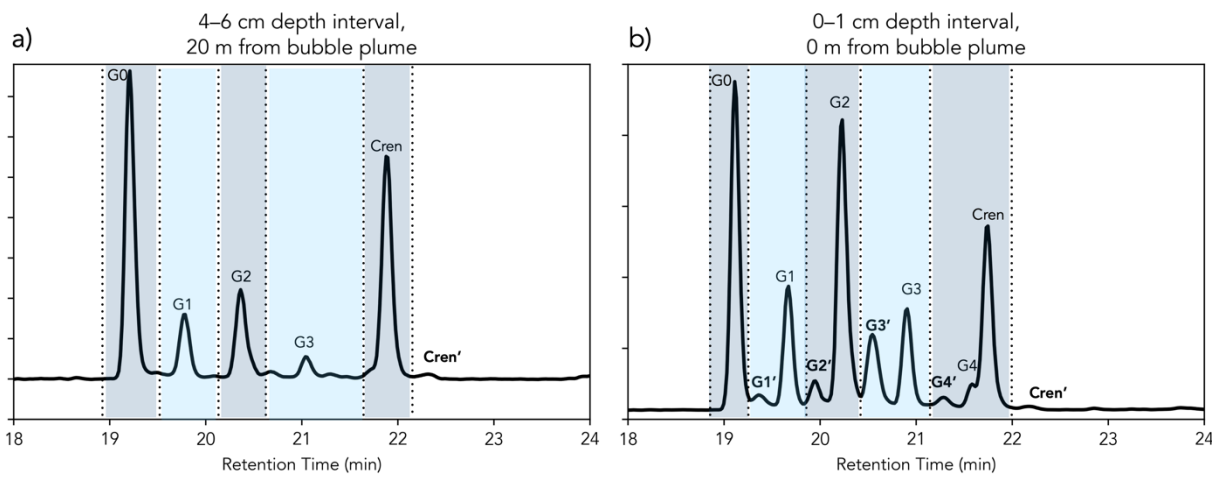
28 In some cases, particularly with isomeric or compositionally complex samples, co-elution can
29 occur, as demonstrated in Figure S1b. If baseline separation of iGDGT peaks is not achieved, closely eluting
30 peaks may be collected in a preceding or succeeding iGDGT peak; this can potentially affect $\delta^2\text{H}$ and $\delta^{13}\text{C}$
31 measurements due to the distinct isotopic signatures of the co-eluting compounds. Due to the complex
32 nature of the samples in the study location, we used simple inverse area- and isotope-mass balance
33 corrections to estimate the degree of co-eluting peaks as detailed in the main text. This is particularly
34 relevant for co-elution of iGDGT-0 and iGDGT-1 fractions and iGDGT-4 and Crenarchaeol fractions.
35 These challenges for complex sedimentary samples highlight the demand for improving chromatographic
36 resolution through further optimization of HPLC methods in cases where benthic sedimentary and methane-
37 cycling influences are significant.

39 2b. iGDGT compound structures and biochemical stoichiometry of biphytanes. Each iGDGT
40 is defined by the number of cyclopentane rings incorporated into the structure. These iGDGTs are
41 composed of two C₄₀ biphytanyl chains, with various underlying structural combinations (Figure S2a,b).
42 For some iGDGTs, specifically iGDGT-2, -3, and -4, multiple theoretical combinations of biphytane chains
43 can yield the same number of total cyclopentane rings for a single iGDGT; these different structural
44 combinations could have potentially distinct isotopic characteristics. This structural variability may reflect
45 differences in compound production by distinct archaeal communities, potentially influenced by differences
46 in biosynthetic pathways, physiological, and/or environmental conditions.

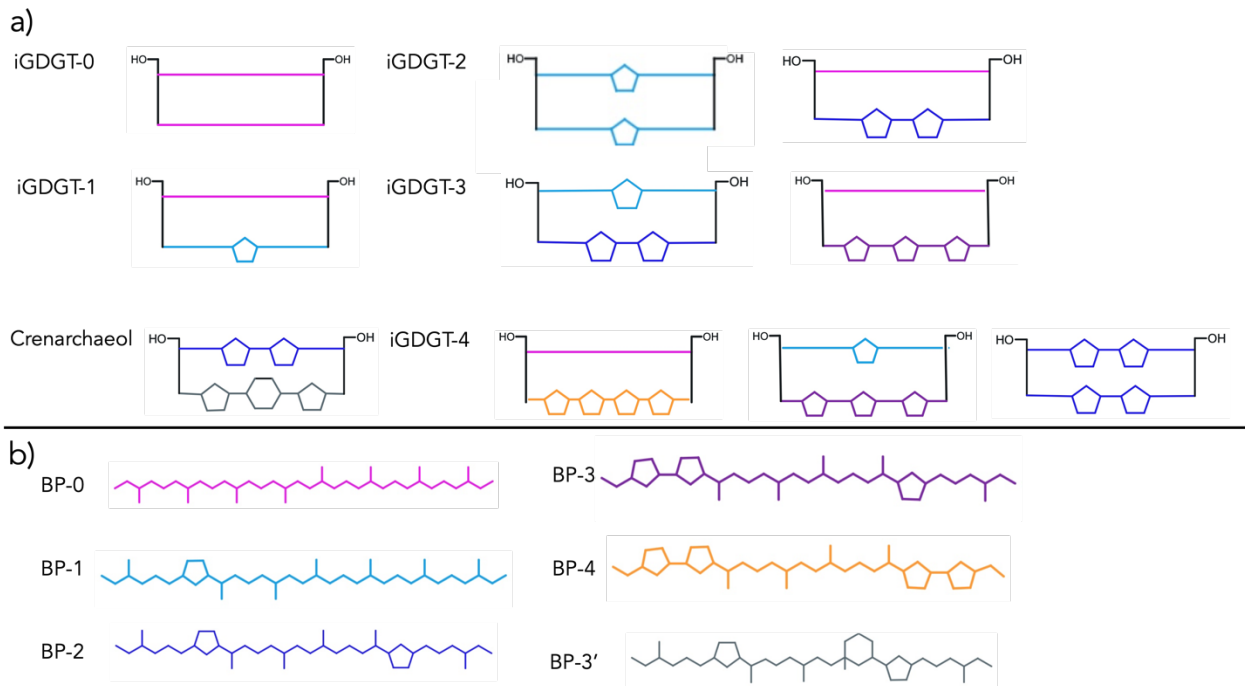
48 **3. Table S1.** Model performance. Differences between observed and predicted $\delta^2\text{H}$ values; mean average
 49 error (MAE) is 11‰. Outliers and all data from sample S7 were omitted from model analysis. The
 50 planktonic fraction is calculated using Equs. 1-3.

Sample	GDGT	Biphytane	Planktonic fraction	Observed $\delta^2\text{H}$ (‰)	Modeled $\delta^2\text{H}$ (‰)
S1	Cren	BP-2	0.95	-302	-297
S1	Cren	BP-3 (Cren)	0.95	-284	-308
S1	G0	BP-0	0.85	-302	-295
S1	G2	BP-0	0.18	-199	-238
S1	G2	BP-1	0.18	-215	-225
S4	Cren	BP-2	0.94	-299	-296
S4	Cren	BP-3 (Cren)	0.94	-291	-308
S4	G0	BP-0	0.63	-297	-276
S4	G2	BP-0	0.16	-255	-236
S4	G2	BP-1	0.16	-224	-225
S5	Cren	BP-2	0.91	-295	-295
S5	Cren	BP-3 (Cren)	0.91	-297	-308
S5	G0	BP-0	0.44	-278	-260
S5	G1	BP-0	0.31	-245	-249
S5	G1	BP-1	0.31	-222	-228
S5	G2	BP-0	0.06	-238	-227
S5	G2	BP-1	0.06	-210	-223
S5	G2	BP-2	0.06	-225	-229
S9	Cren	BP-2	0.91	-289	-295
S9	Cren	BP-3 (Cren)	0.91	-299	-308
S9	G0	BP-0	0.81	-316	-291
S9	G2	BP-0	0.03	-237	-225
S9	G2	BP-1	0.03	-231	-223
S9	G2	BP-2	0.03	-215	-226
S9	G3	BP-1	0.10	-221	-224
S9	G3	BP-2	0.10	-219	-232
S10	Cren	BP-2	0.84	-286	-291
S10	Cren	BP-3 (Cren)	0.84	-305	-308
S10	G0	BP-0	0.80	-315	-290
S10	G1	BP-0	0.25	-263	-243
S10	G1	BP-1	0.25	-234	-227
S10	G2	BP-0	0.08	-235	-229
S10	G2	BP-1	0.08	-217	-223
S10	G2	BP-2	0.08	-216	-232
S11	Cren	BP-2	0.78	-277	-287
S11	Cren	BP-3 (Cren)	0.78	-295	-308
S11	G0	BP-0	0.79	-313	-290
S11	G1	BP-0	0.16	-257	-236
S11	G1	BP-1	0.16	-230	-225
S11	G2	BP-0	0.02	-233	-224
S11	G2	BP-1	0.02	-228	-223
S11	G2	BP-2	0.02	-217	-225
S11	G3	BP-1	0.03	-213	-223
S11	G3	BP-2	0.03	-216	-226

52 **4. Figures**

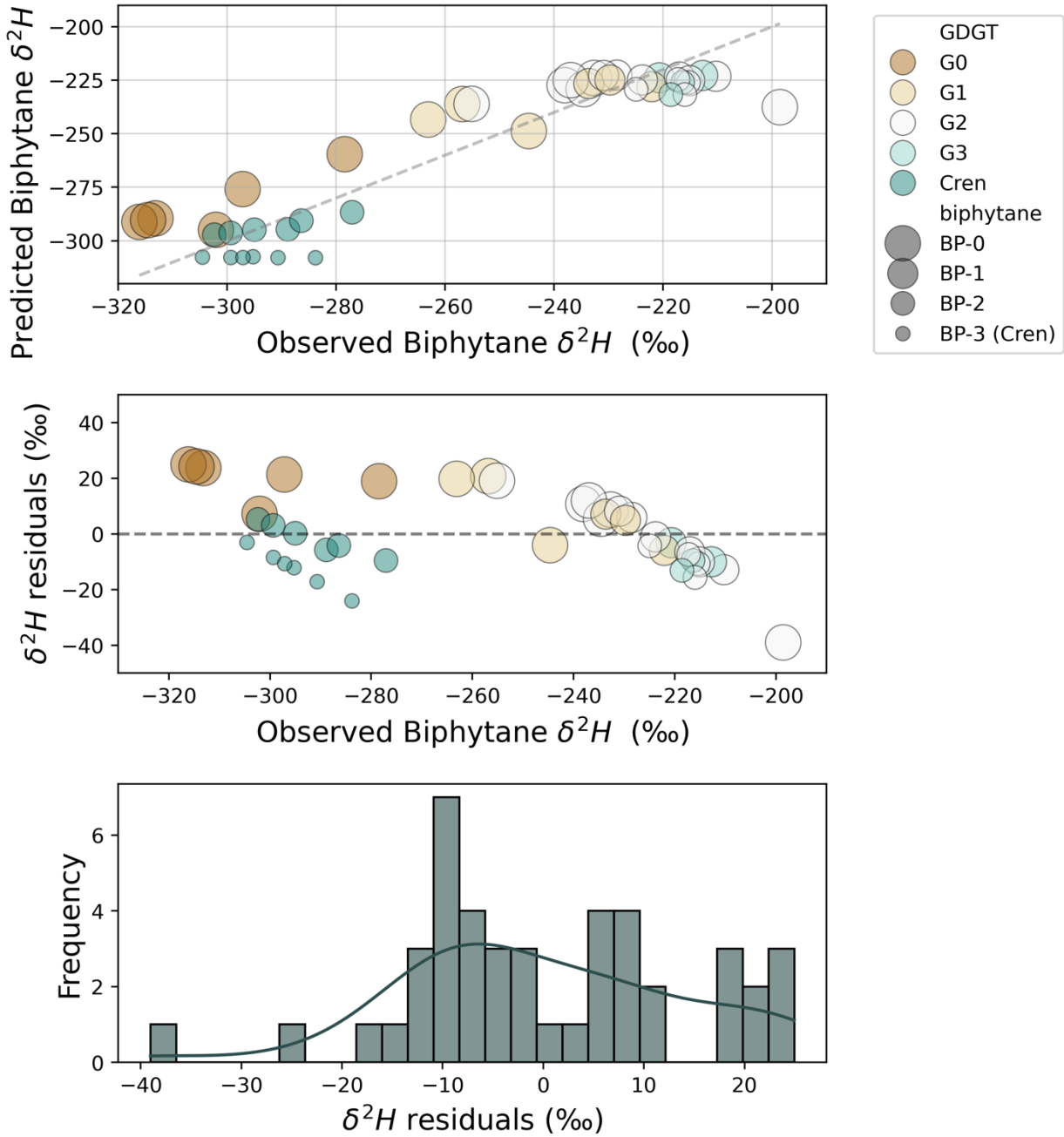


53 **Figure S1.** Example chromatograms from Astoria Canyon samples analyzed using normal-phase high-
54 performance liquid chromatography (NP-HPLC), collected at varying depths and distances from a methane
55 bubble plume at Astoria Canyon, Cascadia Margin (Keller et al., 2025). **a)** Example of baseline separation
56 of iGDGTs based on their elution times. **b)** Example chromatogram of a complex mixture with iGDGT
57 isomers (denoted by ' symbol), which complicates baseline separation of preceding and succeeding iGDGT
58 peaks. Incomplete separation between isomers and main iGDGT peaks may result in co-elution or co-
59 collection of compounds. Gray and blue shading and dashed lines indicate approximate time windows used
60 for collecting individual compounds. The y-axis for both panels a) and b) are relative ion abundance.
61



62
63
64
65
66
67
68
69

Figure S2. Structures of iGDGTs and biphytane components. **a)** Schematic representation of iGDGT compounds and their possible biphytane combinations. Each iGDGT consists of two C₄₀ biphytanyl chains ether-linked to glycerol backbones, depicted by black lines and terminal hydroxyl groups. The differently colored biphytanes represent simplified structures, distinguished by the number of cyclopentane rings or a cyclohexane ring in the case of crenarchaeol. **b)** Structures of the individual biphytanes shown in panel **a** that make up the various iGDGTs.



70
71 **Figure S3.** Top panel: Comparison of the observed and predicted δ^2H values. The dashed line represents a
72 1:1 trend line. Middle Panel: Residuals between modeled and observed δ^2H values. Bottom panel:
73 Histogram of the residuals showing the calculated difference in predicted and observed δ^2H values. The
74 core structures of iGDGTs and BPs are abbreviated with the numbers denoting the number of internal
75 cyclopentane rings; BP-3' refers to the structure containing a cyclohexane ring and crenarchaeol is
76 abbreviated to Cren (Schouten et al., 2002, 2013).
77
78
79
80
81

82 **5. References.**

- 83
- 84 Keller, K.J., Baum, M.M., Liu, X.L., Ashing-Giwa, K., Baker, I.R., Blewett, J., Pearson, A., 2025.
85 Constraining the sources of archaeal tetraether lipids in multiple cold seep provinces of the Cascadia
86 Margin. *Organic Geochemistry* 200.
- 87 Pearson, A., Hurley, S. J., Walter, S. R. S., Kusch, S., Lichtin, S., & Zhang, Y. G. (2016). Stable carbon
88 isotope ratios of intact GDGTs indicate heterogeneous sources to marine sediments. *Geochimica et
89 Cosmochimica Acta*, 181, 18-35.
- 90 Schouten, S., Hopmans, E.C., Schefuß, E., Sinninghe Damsté, J.S., 2002. Distributional variations in
91 marine crenarchaeotal membrane lipids: A new tool for reconstructing ancient sea water
92 temperatures? *Earth and Planetary Science Letters* 204, 265–274.
- 93 Schouten, S., Hopmans, E.C., Sinninghe Damsté, J.S., 2013. The organic geochemistry of glycerol dialkyl
94 glycerol tetraether lipids: A review. *Organic Geochemistry* 54, 19–61.
- 95